Wall-modeled Large-eddy Simulation Based on Building-block Flows

by

Yuenong Ling

B.S.E, Mechanical Engineering, Shanghai Jiao Tong University (2021)
B.S.E, Engineering Physics, University of Michigan (2021)

Submitted to the Department of Aeronautics and Astronautics
in partial fulfillment of the requirements for the degree of

Master of Science in Aeronautics and Astronautics

at the

MASSACHUSETTS INSTITUTE OF TECHNOLOGY

September 2023

© Yuenong Ling. All rights reserved.

Authored by: Yuenong Ling
             Department of Aeronautics and Astronautics
             Aug 15, 2023

Certified by: Adrián Lozano-Durán
              Draper Assistant Professor of Aeronautics and Astronautics
              Thesis Supervisor

Accepted by: Jonathan P. How
             R. C. Maclaurin Professor of Aeronautics and Astronautics
             Chair, Graduate Program Committee

Wall-modeled Large-eddy Simulation Based on Building-block Flows

by

Yuenong Ling

Submitted to the Department of Aeronautics and Astronautics
on Aug 15, 2023, in partial fulfillment of the
requirements for the degree of
Master of Science in Aeronautics and Astronautics

Abstract

A unified subgrid-scale (SGS) and wall model — the building-block flow model (BFM) — for wall modeled large-eddy simulation (WMLES) is proposed by devising the flow as a collection of building blocks that enables the prediction of the eddy viscosity. The core assumption of the model is that simple canonical flows contain the essential physics to provide accurate predictions of the SGS tensor in more complex flows. The model is constructed to predict zero-pressure-gradient wall-bounded turbulence, adverse/favorable pressure gradient effects, separation and laminar flow. The approach is implemented using a Bayesian classifier, which identifies the contribution of each building block in the flow, and a neural-network-based predictor, which estimates the eddy viscosity based on the building-block units. The training data are directly obtained from wall-modeled LES with an exact SGS/wall model for the mean quantities to guarantee consistency with the numerical discretization. The model is validated in canonical flows, the NASA High-Lift Common Research Model and a Gaussian bump and shown to improve the predictions with respect to current modeling approaches. The modular extensibility of the BFM paradigm will allow for future improvements by incorporating additional physics.

Thesis advisor: Adrián Lozano-Durán
Title: Draper Assistant Professor of Aeronautics and Astronautics

Acknowledgments

First and foremost, I would like to express my deepest gratitude to my advisor, Professor Adrián Lozano-Durán, for his invaluable guidance and unwavering support throughout this research endeavor. His brilliance and profound understanding of turbulence theory has been an inspiration. I am especially appreciative of his thoughtful suggestions that have enriched not only my academic journey but also my personal growth. His passion for exploring new research directions also motivates me tremendously. I eagerly look forward to continuing our collaboration in the future.

I would also like to extend my sincere thanks to all members of the Computational Turbulence Research Group. Their assistance and encouragement have been instrumental to the completion of this project. In addition, I am grateful to my office mates for making the past two years so memorable with their friendship.

This research work originated from a summer program project at the Center for Turbulence Research at Stanford. I am especially thankful for the guidance of my collaborator and good friend Gonzalo during this impactful experience. I also wish to acknowledge Konrad and Kevin for their valuable suggestions over the course of the program. I remain appreciative of the friendship forged with program participants including Di, Andrew, Tony and Leon, who made that summer remarkably enjoyable.

Most importantly, I wish to thank my family for their unconditional love and support over the past two years. Despite physical distance, their emotional encouragement has been invaluable in helping me complete this journey. I could not have accomplished this without them.

Finally, I would like to thank the National Science Foundation and CTR summer program for their financial support for this research project and MIT SuperCloud and Lincoln Laboratory Supercomputing Center for providing HPC resources.

THIS PAGE INTENTIONALLY LEFT BLANK

Contents

THIS PAGE INTENTIONALLY LEFT BLANK

List of Figures

List of Tables

Chapter 1

Introduction

Turbulence is a complex phenomenon that has been the subject of incessant attempts to fully understand and model its properties over the last century. Recent advancements in computing power have played a pivotal role in enabling the adoption of computational fluid dynamics (CFD) as a crucial tool for both fundamental research and engineering design involving turbulence. Concurrently, the progress in machine learning algorithms has facilitated wide-ranging applications of these techniques across various fields. Leveraging the wealth of data obtained from CFD, machine learning has emerged as a promising approach for turbulence modeling. The present thesis proposes and evaluates a novel turbulence model based on machine learning to address key issues for CFD's applicability in engineering applications.

1.1   CFD and Wall-bounded Turbulence

The ability to accurately simulate complex flows using CFD is crucial in many applications, ranging from aircraft design to drag reduction in pipelines [1, 2]. Most flows in these cases involve wall-bounded turbulence, where one or more solid walls are present. A significant challenge arises when simulating such flows: the computational requirements increase as finer details of flow eddies near the wall need to be captured. This can be quantitatively understood by considering the near-wall small-scale motions (i.e., quasi-streamwise vortices), whose size scales with the vis-

cous length scale $\delta_\nu = \nu/u_\tau$, where ν is the kinematic viscosity and $u_\tau = \sqrt{\tau_w/\rho}$ is the frictional velocity based on wall shear stress. The length scale δ_ν is directly associated with the friction Reynolds number, given by $Re_\tau = u_\tau \delta/\nu$, where δ represents the relevant length scale. As the Reynolds number becomes increasingly large, δ_ν diminishes, leading to prohibitively expensive grid resolutions. Therefore, direct numerical simulation (DNS), which resolves all the scales of motion, is not feasible for these applications.

As directly resolving all the scales represented by these eddies is impractical, researchers and engineers resort to other methods to capture the physics of flow. One widely adopted approach is based on Reynolds-averaged Navier-Stokes (RANS) equations. These equations are obtained by averaging the Navier-Stokes (NS) equations over ensembles (different realizations of flows), thereby only capturing the average quantities of the flow. Formally, the velocity field $\mathbf{u}(\mathbf{x}, t)$ is decomposed into the mean and fluctuation components as follows:

$$\mathbf{u}(\mathbf{x}, t) = \langle \mathbf{u}(\mathbf{x}, t) \rangle + \mathbf{u}'(\mathbf{x}, t), \tag{1.1}$$

where $\langle \cdot \rangle$ is the operator for ensemble average. For incompressible flow, RANS equations are derived by applying the Reynolds decomposition described by Equations 1.1 to NS equations and can be expressed as:

$$\frac{\partial \langle u_i \rangle}{\partial x_i} = 0, \tag{1.2}$$

$$\frac{\partial \langle u_j \rangle}{\partial t} + \langle u_i \rangle \frac{\partial \langle u_j \rangle}{\partial x_i} = \nu \frac{\partial^2 \langle u_j \rangle}{\partial x_i \partial x_i} - \frac{\partial \left\langle u_i' u_j' \right\rangle}{\partial x_i} - \frac{1}{\rho} \frac{\partial \langle p \rangle}{\partial x_j}, \tag{1.3}$$

where the additional term compared to the original the NS equations contains a new unclosed tensor called the Reynolds stress $-\langle u_i' u_j' \rangle$.

Modeling the unclosed Reynolds stress tensor is the central topic of turbulence modeling. One limitation of Reynolds-averaged Navier-Stokes (RANS) modeling is its steady nature, which makes it inadequate for flows where statistical unsteadiness plays a significant role. In such cases, RANS models provide inaccurate estimations,
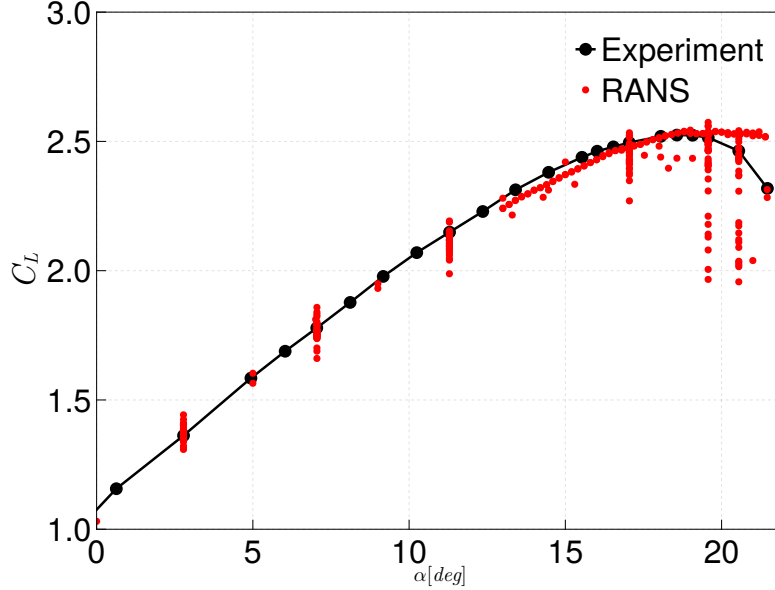
Figure 1-1: RANS results for lift coefficients C_L as a function of angles of attack α submitted for the Third High Lift Prediction Workshops. See more details in [6].

even for mean quantities [3]. While efforts have been put into modeling unsteadiness by using Reynolds transport equations, its accuracy and convergence characteristics in these situations is still in doubt. This issue is particularly relevant for aircraft operating in take-off and landing configurations, characterized by large angles of attack (AoAs) and substantial lift generation. The occurrence of massive separation in these cases further emphasizes the importance of unsteadiness [4].

In the recently held Third High Lift Prediction Workshops, RANS-based solvers yield a range of results that deviate from experimental data, as illustrated in Figure 1-1. In another study, even state-of-the-art RANS solvers with closure models tailored for the corner flow produce $\mathcal{O}(1)$ errors for wing-body juncture flows, which are crucial for the accurate prediction of the whole airplane [5]. Such misalignment showcases the desperate need for an alternative method capable of accounting for unsteady flow.

A natural alternative is large-eddy simulation (LES), where only large-scale energy-containing eddies are resolved. In LES formulation, a filtering operation is applied to the flow field to filter out small-scale features. The contribution of small eddies, so-called subgrid-scale stress (SGS), is modeled [7]. LES has shown its capability in accurately modeling turbulence for canonical flows such as homogeneous isotropic

turbulence. However, similar to DNS, LES still requires the resolution of near-wall eddies to capture the correct dynamics of wall-bounded turbulence. Therefore, while LES reduces the grid requirements for regions away from the wall, it does not fully address the fundamental challenge of expensive simulations due to the need to resolve near-wall dynamics.

To capture the unsteady nature of flow while also maintaining a manageable degree of freedom for real applications, hybrid methods have been proposed. These methods combine elements of both LES and RANS or other simplifications to address different regions of the flow. Two prominent blending approaches are detached-eddy simulation (DES) and wall-modeled large-eddy simulation (WMLES) [8]. While both aiming to replace boundary layer with some forms of simplified models, DES and WMLES differ in their treatment on the outer layer. Namely, DES models both outer and inner layers of the boundary layer, whereas WMLES only models the inner layer. In more complex flow scenarios, WMLES resolves energetically important regions to a greater extent than DES [9]. This thesis will primarily focus on WMLES. For readers interested in DES or other unsteady extensions of RANS, comprehensive reviews can be found in [10, 11].

1.2 Wall-modeled Large-eddy Simulation

WMLES approaches can be generally divided into two categories: hybrid LES/RANS formulations and wall-stress model approaches. The hybrid LES/RANS formulation follows the principle of DES to use RANS in the inner layer of the boundary layer and LES in other regions. The treatment of blending these two computational domains at certain height $y = h_{wm}$ could be nontrivial and often leads to problems such as log-layer mismatch [12]. In practice, it is also often challenging to implement both solvers and run them simultaneously. This thesis, therefore, will focus on the wall-stress model approach, which is more straightforward to implement and has been shown to be effective in many applications [13].

The gist of wall-stress models is to impose wall shear stress τ_w as a boundary

condition based on the information of the flow at certain height from the wall [9]. For incompressible flow, Figure 1-2 shows a sketch of how a wall model works. Concrete approaches to infer the correct boundary condition include math-based (filter-based, control-theory, ...) and physics-based (algebraic, ordinary differential equations (ODE), partial differential equations (PDE), ...) methods [9].
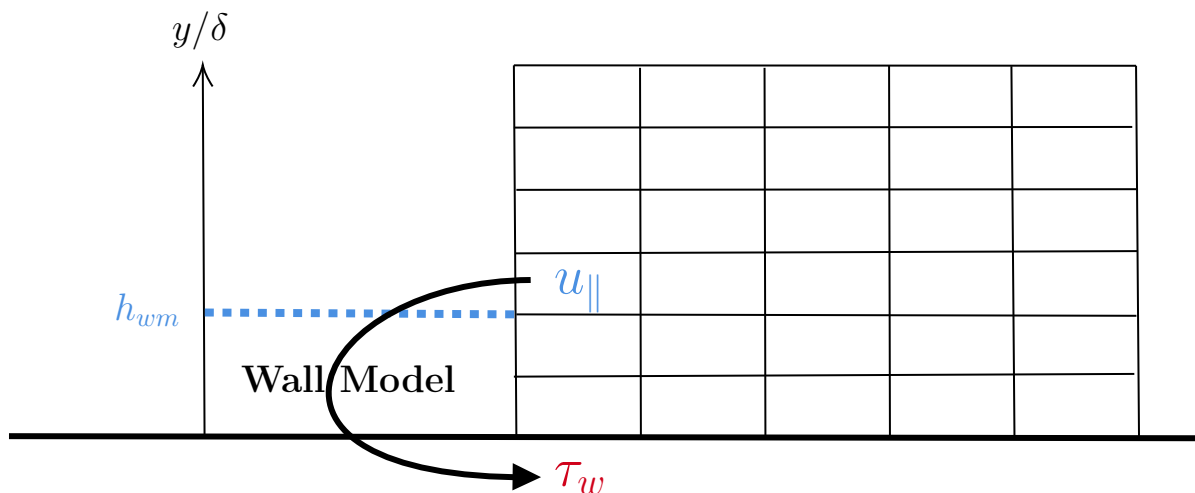
Figure 1-2: The principle of wall-stress models for incompressible flow. The instantaneous wall-parallel velocity $u_{\parallel}$ is fed into the wall model to infer the wall shear stress τ_w serving as the boundary condition.

We can examine the grid-point and time-step requirements as estimated by Yang and Griffin [14], who based their work on classical estimations by Chapman and following corrections by Choi and Moin [15, 16]. According to their findings, the scaling laws for DNS, LES, and WMLES are $Re_{L_x}^{2.91}$, $Re_{L_x}^{2.72}$, and $Re_{L_x}^{1.14}$, respectively, where Re_{L_x} represents the Reynolds number based on the length of the flat plate. Therefore, while DNS and LES are computationally infeasible, WMLES is computationally competitive to other CFD approaches with lower fidelity. Indeed, recent studies by Goc et al. have shown that WMLES is close to achieve the accuracy and turnaround times demanded by the aerospace industry [17]. While state-of-the-art WMLES performs satisfactorily in turbulent boundary layers with sufficient grid resolution, its performance deteriorates in the presence of less than 20 grid points per boundary layer thickness. Unfortunately, the latter grid resolution is typical for external aerodynamics applications [18]. To this end, we aim to improve the performance of WMLES in

the presence of coarse grids by improving the modelling of SGS and wall shear stress.

1.3 Machine Learning for Turbulence Modeling

While traditional turbulence modeling focuses on physics-based arguments and empirical calibration of model parameters, recent explosion in high-fidelity data and machine-learning tools enables the application of new data-intensive techniques. There are already extensive applications of machine learning in fluid mechanics and the reader is referred to the review by Brunton et al. [19]. While promising, modeling using machine learning still faces important challenges. As summarized in [20], most salient problems include how to correctly use the data set, how to account for the difference between learning environment (usually DNS data) and injection environment (RANS or LES), how to apply physical and mathematical constraints, and how to provide the confidence of the model. While it is challenging to solve these problems all at once, it is worth designing a framework that can address at least some of them to enhance the current paradigm. These challenges must be kept in mind when designing new machine learning-based turbulence models.

For LES specifically, machine learning has been applied for both SGS modeling and wall models. For instance, SGS models have been trained using data from filtered DNS [21, 22]. Examples of supervised learning for wall modeling include [23], [24], [25] and [26], to name a few. Interestingly, most studies to date have trained the model with data from higher-fidelity simulations, such as DNS or wall-resolved LES. As a consequence, previous models ignored the nonnegligible errors arising from the numerical discretization in actual WMLES. This corresponds to the challenge of accounting for the inconsistency between the learning and injection environments. Unfortunately, not many attempts have been aimed at solving this issue. An exception is the work by Bae et al. using reinforcement learning [27].

Another major issue from previous studies is the lack of generalizability of the model. Many machine learning-based models are often tailored and trained specifically for a particular flow configuration, such as channel flow, pipe flow, or flow in a

periodic hill. While this specialization can yield higher accuracy within the trained configuration, it becomes impractical and inefficient to create a new model for each distinct flow scenario encountered in practical applications. Furthermore, it has been shown that applying the current model to different flow conditions, e.g., flows with different Reynolds numbers, can lead to significant errors [23].

1.4   Scope and Objective of the Thesis

In this thesis, we aim to devise a unified SGS/wall model called building-block flow model (BFM) that is consistent with the numerical discretization, suitable for various flow physics and applicable to complex geometries. Throughout this thesis, the focus remains on the development and evaluation of the BFM to ensure its practical utility and relevance for engineering tasks. The design of BFM is rooted in the idea that truly revolutionary improvements in WMLES will encompass advancements in numerics, grid generation and wall/SGS modeling. The proposed model architecture is summarized in Figure 1-3. The details of the model are provided in the following chapters. Part of the content of this thesis has been published in [28], [29] and [30].

The thesis is organized as follows: Chapter 2 describes the numerical method and machine learning tools used. Chapter 3 introduces the requirements, assumptions and formulation of the BFM model and also provides the details of the implementation. Chapter 4 presents the results on both canonical flows and complex cases. Chapter 5 offers a discussion on the status quo of the model. Finally, Chapter 6 summarizes the work and provides suggestions for future model improvements.
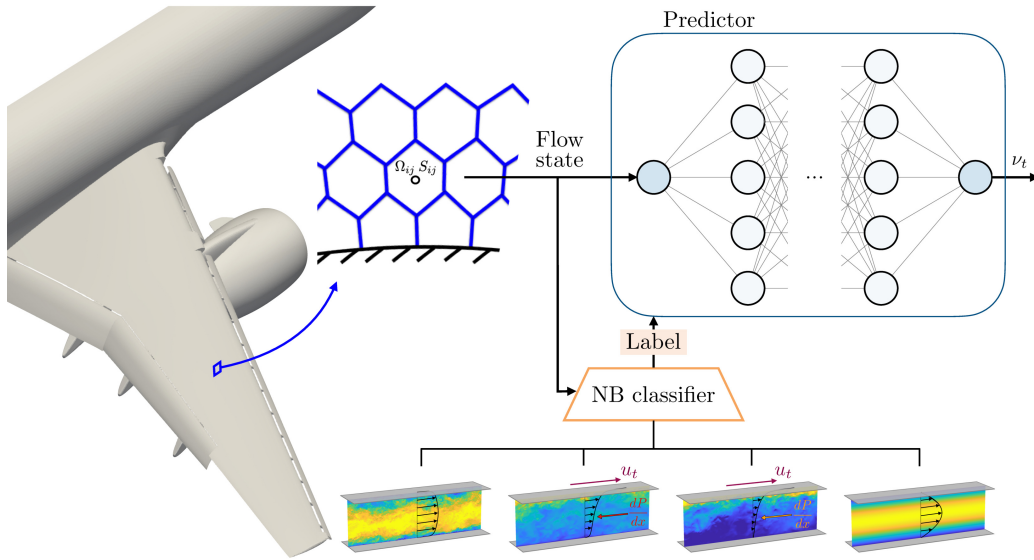
Figure 1-3: Schematic of the building-block flow model. The panel shows the classifier-predictor structure and the architecture of artificial neural network (ANN). The flow state refers to $(I_1, ..., I_6, \nu, \Delta, u_{||})$ and different ANNs are used for the inner and outer layer. The bottom of the figure depicts the building-block flows considered (from left to right): turbulent channel flow with zero pressure gradient, Poiseuille-Couette flow with mild adverse pressure gradient, Poiseuille-Couette flow with separation and laminar Poiseuille flow. The details are provided in following chapters.

Chapter 2

Methods

In this chapter, we present details on numerical methods used in this thesis including the formulation of LES, conventional SGS/Wall models, machine learning tools and numerical solvers.

2.1 Large-eddy simulation

The resulting governing equations after filtering the Navier-Stokes equations are

$$\frac{\partial \overline{u}_i}{\partial x_i} = 0, \tag{2.1}$$

$$\frac{\partial \overline{u}_j}{\partial t} + \overline{u}_i \frac{\partial \overline{u}_j}{\partial x_i} = \nu \frac{\partial^2 \overline{u}_j}{\partial x_i \partial x_i} - \frac{\partial \tau_{ij}^{SGS}}{\partial x_i} - \frac{1}{\rho} \frac{\partial \overline{p}}{\partial x_j}, \tag{2.2}$$

where $\overline{(\cdot)}$ represent filtered quantities and τ_{ij}^{SGS} is the anisotropic residual-stress tensor, also known as the SGS tensor. It is derived from the residual-stress tensor τ_{ij}^R defined as

$$\tau_{ij}^R = \overline{u_i u_j} - \overline{u}_i \, \overline{u}_j, \tag{2.3}$$

subtracted by its trace

$$\tau_{ij}^{SGS} = \tau_{ij}^R - \frac{1}{3} \tau_{ii}^R \delta_{ij}. \tag{2.4}$$

25

The goal of turbulence modeling in the context of LES is to express the tensor τ_{ij}^{SGS} as a function of known quantities.

2.2   Subgrid-scale stress models

In this section, we list some state-of-the-art SGS models deriving from physics grounded theories. These models are used for comparison with the machine learning models in Chapter 4.

2.2.1   Dynamic Smargorinsky Model (DSM)

As one of the mostly adopted SGS models, the Smagorinsky model [31] is an one-equation model that relates the SGS stress to the resolved strain rate following the Boussinesq assumption

$$\tau_{ij}^{\text{SGS}} - \frac{1}{3}\delta_{ij}\overline{S}_{kk} = -2\nu_t\overline{S}_{ij}, \tag{2.5}$$

where ν_t is the eddy viscosity and $\overline{S}_{ij}$ is the resolved strain rate tensor. In the original static version, the eddy viscosity is given by an analogy to the mixing-length hypothesis

$$\nu_t = (C_S\Delta)^2(\overline{S}_{ij}\overline{S}_{ij})^{1/2}, \tag{2.6}$$

where C_S is the Smagorinsky constant and Δ is the grid size. To deal with different flows and regions near the wall, practitioners often need to set different Smagorinsky constants or do *ad hoc* adjustments. With this limitation in mind, Germano et al. proposed a dynamic procedure to dynamically set the coefficient C_S based on local flow characteristics [32]. The rough idea is to apply a second filter on resolved quantities and assume the Smagorinsky model can be applied for the filtered stress. The coefficient then can be found by minimizing procedures. A detailed description of the dynamic procedure can be found in the original paper [32]. Lilly [33] used a least-square technique to improve the robustness and stability of the procedure. The

dynamic Smagorinsky model with Lilly's modification is widely used in LES of wall-bounded flows [34] and is considered one of the most reliable SGS models. Readers are referred to classical textbooks such as [7] for mathematical details of the model.

2.2.2 Vreman Model

While the dynamical Smagorinsky model is well founded in theory, its practical implementations are often nontrivial due to the necessity of explicit filtering operations, ensemble average along homogeneous directions and *ad hoc* clipping of negative eddy viscosity [35]. To remedy this issue, Vreman [36] proposed a new SGS model for shear flow, which is easy to implement and enjoys low dissipation in transitional and near-wall regions. The eddy viscosity given by the Vreman model is

$$\nu_t = c\sqrt{\frac{B_\beta}{\alpha_{ij}\alpha_{ij}}}, \tag{2.7}$$

with

$$\alpha_{ij} = \frac{\partial \bar{u}_j}{\partial x_i},$$

$$\beta_{ij} = \Delta_m^2 \alpha_{mi}\alpha_{mj},$$

$$B_\beta = \beta_{11}\beta_{22} - \beta_{12}^2 + \beta_{11}\beta_{33} - \beta_{13}^2 + \beta_{22}\beta_{33} - \beta_{23}^2.$$

It is reported to be as accurate as the dynamic Smagorinsky model in a lot of applications but with a much lower computational cost [36]. Also, due to its simplicity, the Vreman model can be easily implemented for complex geometries, making it an ideal benchmark for other SGS models.

2.2.3 Anisotropic Minimum Dissipation Model

Verstappen derived a so-called QR model based on the idea that eddy dissipation should be minimized to ensure subgrid scales should be dynamically insignificant [37]. By examining the time evolution equation of the SGS, one can find that the rate of dissipation of resolved kinetic energy due to SGS model, also known as eddy

dissipation, is given by

$$\varepsilon_\tau = -\tau_{ij}\frac{\partial \bar{u}_j}{\partial x_i}. \tag{2.8}$$

The corresponding eddy viscosity is given by

$$v_t = C_\Delta \frac{\max\{r(\bar{u}), 0\}}{q(\bar{u})}, \tag{2.9}$$

where $q(\bar{u})$ and $r(\bar{u})$ are the second and third invariants of resolved rate-of-strain tensor and C_Δ is a model constant. The Anisotropic Minimum Dissipation (AMD) model by Rozema et al. was developed based on QR model to account for anisotropic grids [38]. Again, readers are referred to [38] for details of the model.

2.3 Equilibrium Wall Model

While there are a wide range of wall models available, the most popular choice is an ODE-based equilibrium wall model (EQWM), which will be used throughout the thesis when compared with machine learning-based models. The unresolved inner layer is modeled by solving

$$\frac{d}{dy}\left[(\nu + \nu_{t,\mathrm{wm}})\frac{dU_{\mathrm{wm}}}{dy}\right] = 0, \tag{2.10}$$

where U_{wm} is the wall-parallel velocity at certain given height and $\nu_{t,wm}$ is the local eddy viscosity modeled by the mixing length hypothesis

$$\nu_{t,\mathrm{wm}} = \kappa y \sqrt{\frac{\tau_w}{\rho}} \mathcal{D}, \quad \mathcal{D} = \left[1 - \exp\left(-y^+/A^+\right)\right]^2, \tag{2.11}$$

where $\kappa = 0.41$, $A^+ = 17$, and $\mathcal{D}$ is the Van Driest damping function [9].

2.4 Machine Learning Tools

In this section, we provide a overview of the architecture and methodology of the machine learning tools utilized in this thesis. Additional details including data gen-

eration, choice of training and testing data, and training process are discussed in Chapter 3. As illustrated in Figure 1-3, the machine learning framework used in this thesis consists of two components: a classifier and a predictor. The classifier is used to divide the flow field into different categories. The predictor subsequently estimates the necessary quantities for simulations.

2.4.1 Classifier

A Naive Bayes (NB) classifier is employed to classify the flow field into different categories. The NB classifier is a probabilistic classifier that applies Bayes' theorem with strong (naive) independence assumptions [39].

Let us consider the classification of observed vectors $(x_1, x_2, \cdots, x_n)^T$ into K classes denoted as $C_1, \cdots, C_K$. The independence assumptions made by the NB classifier assert that the presence of a feature x_i is independent of any other feature x_j for $j \neq i$ within each class. Mathematically, this can be expressed as follows:

$$p(x_1, x_2, \cdots, x_n | C_k) = \prod_{i=1}^{n} p(x_i | C_k) \quad \text{for } k = 1, \cdots, K. \quad (2.12)$$

The NB classifier then predicts the category C_k with the highest posterior probability given the observed vector. The NB classifier is chosen for its simplicity and efficiency, making it a suitable choice for the classification task in this study.

2.4.2 Predictor

Fully connected feedforward artificial neural networks (ANN), also known as multi-layer perceptrons (MLP), are employed to predict the necessary quantities for simulations. The MLP, known as a universal approximator [40], possesses the theoretical capability to approximate any continuous function with arbitrary precision. In practice, however, the MLP is limited by the choice of activation functions, the number of hidden layers and the number of neurons in each hidden layer. The training of the MLP involves minimizing a loss function, which quantifies the difference between the predicted value and the true value. In this thesis, MLP is only used to carry out

regression tasks. As demonstrated in Figure 2-1, it aims to find a mapping between input and output variables.
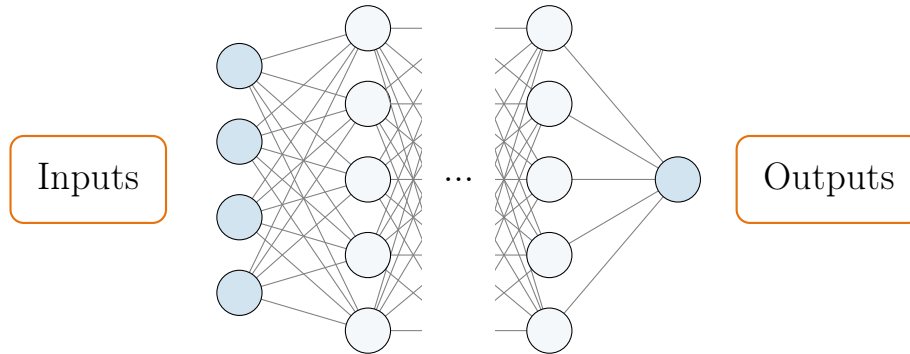
Figure 2-1: A fully connected neural network used for regression tasks.

2.5   Numerical solvers

Two numerical solvers are used in this thesis: an in-house finite-difference solver and a finite-volume solver charLES.

The in-house solver uses a spatial discretizaion of the incompressible Navier–Stokes equations with a staggered second-order-accurate finite difference method [41]. For time advancement, an explicit third-order-accurate Runge–Kutta method is employed [42]. Periodic boundary conditions are imposed in homogeneous directions, while the no-slip condition is enforced at the walls. The code has been validated in various studies for turbulent channel flows [18, 43]. The in-house solver will be denoted as FD.

CharLES is a finite-volume, second-order-accurate, compressible flow solver developed by Cascade Technologies, Inc. It utilizes a low dissipation scheme to spatial discretization to cater it for coarsely resolved large eddy simulations [17]. Also, a Voronoi diagram-based mesh generation method is adopted to generate high-quality meshes. A sample grid generated for flow with complex geometry (CRM-HL to be introduced) is shown in Figure 4-7 in Chapter 4. Readers are referred to [44] for more

details about charLES.

THIS PAGE INTENTIONALLY LEFT BLANK

Chapter 3

Building-block Flow Model

This chapter discusses the formulation of the building-block flow model (BFM). The concept of BFM follows directly from the earlier work by Lozano-Duran et al. [45, 46], but it extends the original wall model to a unified SGS/wall model. It is worth noting that two versions of BFMs, namely BFM v0.1.0 and BFM v0.2.0, will be presented herein. The primary distinction between these two models lies in the fact that BFM v0.2.0 is specifically tailored for implementation with the charLES solver and does not currently incorporate a classifier. Unless specified, details specified in the following sections apply to both versions.

3.1 Requirements

In the introduction, we briefly discussed the overarching goals of the current unified SGS/wall model. In this section, we elaborate on the requirements that the model should satisfy to achieve these goals. We also present the corresponding solutions that we have developed to meet these requirements.

(I) The unified SGS/wall model must be able to deal with complex geometries (e.g., realistic aircraft). Consequently, the model's inputs must be restricted to local information, namely variables that are spatially localized. This limitation ensures that the model operates effectively in diverse and complex geometries,

where the availability of global information may be limited or impractical to obtain.

(II) The model must account for numerical errors stemming from the inconsistency between learning and injection environments. To address this concern, the data generation method should guarantee that the data source remains consistent with the intended application. The model then can effectively account for and mitigate any numerical errors that may arise due to inconsistencies between these settings.

(III) The model must be generalizable to different flow regimes (e.g. different Reynolds number). To achieve this, the normalization of data is of key importance.

(IV) The model must be readily applicable to different flow physics. In order to achieve this, it is necessary to employ different building-block flows during the model training process.

(V) The inputs and outputs must be dimensionally consistent. To accomplish this, all data utilized in the model are nondimensionalized by employing appropriate scaling variables. Nondimensionalization allows for a consistent representation of the input and output variables, ensuring compatibility and coherence throughout the model.

(VI) The model must be invariant under translation, rotation and Galilean transformation. The current model addresses this requirement by utilizing the invariants of the velocity gradient tensor directly. The upcoming section will provide a comprehensive explanation of the process employed to incorporate the invariants into the model.

3.2   Assumptions

To develop the model, several key assumptions are made, outlined as follows:

(I) The local state of a flow field can be classified into a finite set of canonical flows, and its behavior closely resembles one of these canonical flows.

(II) Non-dimensionalized inputs from local states are enough for predicting the required subgrid-scale stress and wall shear stress.

(III) Appropriate scalings exist that enable the non-dimensionalization of both inputs and outputs, thereby enhancing the model's generalizability.

(IV) The wall shear stress required by the wall model can be estimated using a local eddy viscosity at the wall.

(V) The SGS tensor is a function of resolved rate-of-strain tensor and rotation tensor.

The model introduced in this study relies on these assumptions to establish its theoretical foundation. The validity of each assumption will be examined and discussed in the subsequent chapter to ensure a comprehensive evaluation of the model's robustness and limitations.

3.3   Building-block Flows

We consider four types of building-block flows, viz., laminar channel flow, fully developed turbulent channel flow with zero pressure gradient (ZPG), turbulent Poiseuille-Couette flow with mild adverse pressure gradient (PC2) and turbulent Poiseuille-Couette flow close to separation (PC0) as summarized in Figure 3-1. For BFM v.0.2.0, the laminar channel flow is not included. In all building blocks considered, x, y and z correspond to the streamwise, wall-normal and spanwise directions, respectively. The distance between the top and bottom wall in the channel is $2h$. In the case of turbulent and laminar channel flows, both walls are stationary. For Poiseuille-Couette flows, the bottom wall remains fixed, while the upper wall moves at a constant streamwise velocity u_t. Irrespective of the flow type, the friction Reynolds numbers are defined
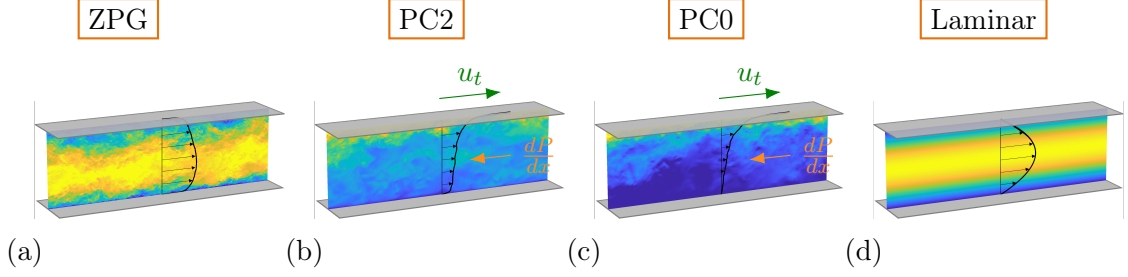
Figure 3-1: The building-block flows considered (from left to right): turbulent channel flow with zero pressure gradient (ZPG), Poiseuille-Couette flow with mild adverse pressure gradient (PC2), Poiseuille-Couette flow with separation (PC0) and laminar Poiseuille flow.

as follows:

$$Re_\tau = \frac{u_\tau h}{\nu},\tag{3.1}$$

where u_τ is determined by the wall shear stress at the bottom wall.

The rationale of including these four building-block flows is as follows.

1. Turbulent channel flows with zero pressure gradient are widely regarded as a fundamental and extensively studied canonical flow for wall-bounded turbulence. Due to their well-defined and controlled nature, turbulent channel flows have served as a standard benchmark for studying turbulent wall-bounded flows. It is expected that a model trained on turbulent channel flows can demonstrate a high level of applicability and transferability to other attached turbulent wall-bounded flows.

2. Turbulent channel flows with varying pressure gradients are utilized to replicate the adverse pressure gradient commonly encountered in real-world applications. By gradually increasing the magnitude of the adverse pressure gradient, the model can capture the critical transition from attached to separated flow, allowing for a comprehensive understanding of the dynamics and characteristics associated with flow separation. This broad range of flow conditions close to separation enables the model to better predict and account for separation phenomena. The ability to control and manipulate the magnitude of the adverse pressure gradient ensures that the model encompasses a wide spectrum of flow

36

conditions, enhancing its predictive capabilities.

To quantify the intensity of the adverse pressure gradient, a pressure gradient-based Reynolds number (Re_p) is introduced. The Re_p is defined as:

$$Re_p = \frac{\sqrt{h^3/\rho \frac{dP}{dx}}}{\nu}, \tag{3.2}$$

where $\frac{dP}{dx}$ denotes the streamwise pressure gradient. The Re_p provides a measure of the strength of the adverse pressure gradient, with larger values indicating a more pronounced adverse pressure gradient. By incorporating cases with different Re_p into the training set, the model can effectively gauge and categorize different levels of adverse pressure gradients.

3. The inclusion of laminar channel flows is crucial for the model's ability to accurately predict wall shear stress in the laminar regime. This is important to ensure that the model performs accurately in the free-stream region where laminar flow conditions prevail. By incorporating laminar channel flows, the model can effectively account for the unique features and shear stress patterns observed in the laminar regime.

Note that for BFM v0.2.0, we do not include laminar channel flow because a classifier has not been implemented yet. The inclusion of the laminar case without a classifier may have negative impacts on the model's performance. The classifier will be incorporated in the future.

3.4 Formulation

One of the key assumptions we have made is the assumption (V). Mathematically, it assumes a functional form

$$\tau_{ij}^{SGS} = f(\bar{S}_{ij}, \bar{R}_{ij}), \tag{3.3}$$

where the resolved rate-of-strain and rotation tensors are defined as

$$\bar{S}_{ij} = \frac{1}{2}\left(\frac{\partial \bar{u}_i}{\partial x_j} + \frac{\partial \bar{u}_j}{\partial x_i}\right), \ \bar{R}_{ij} = \frac{1}{2}\left(\frac{\partial \bar{u}_i}{\partial x_j} - \frac{\partial \bar{u}_j}{\partial x_i}\right). \tag{3.4}$$

By applying Caley-Hamilton theorem, it can be shown that the deviatoric part of the resolved stress can be represented as a linear combinations of only five tensors

$$\begin{aligned}\boldsymbol{\tau}^{SGS} =& C_1\Delta^2|\mathbf{S}|\mathbf{S} + C_2\Delta^2\left(\mathbf{S}^2\right)^d + C_3\Delta^2\left(\mathbf{R}^2\right)^d + \\ & C_4\Delta^2(\mathbf{SR} - \mathbf{RS}) + C_5\Delta^2\frac{1}{|\mathbf{S}|}\left(\mathbf{S}^2\mathbf{R} - \mathbf{RS}^2\right),\end{aligned}$$

where C_i are undetermined coefficients and $(\cdot)^d$ indicates the trace-free part of the tensor [47]. The coefficients C_i are functions of the six invariants

$$\begin{aligned}I_1 &= \mathrm{tr}\left(\bar{\mathbf{S}}^2\right), & I_2 &= \mathrm{tr}\left(\bar{\mathbf{R}}^2\right), \\ I_3 &= \mathrm{tr}\left(\bar{\mathbf{S}}^3\right), & I_is &= \mathrm{tr}\left(\bar{\mathbf{S}}\bar{\mathbf{R}}^2\right), \\ I_5 &= \mathrm{tr}\left(\bar{\mathbf{S}}^2\bar{\mathbf{R}}^2\right), & I_6 &= \mathrm{tr}\left(\bar{\mathbf{S}}^2\bar{\mathbf{R}}^2\bar{\mathbf{S}}\bar{\mathbf{R}}\right). \end{aligned} \tag{3.5}$$

These invariants, originally proposed by Pope, are invariant under rotation, and are therefore suitable for the model to be applied to flows with arbitrary orientations [48]. The current form used in this thesis can be found in [47].

While it is theoretically possible to explore all five functional forms,

$$C_i = f_i(I_1, I_2, I_3, I_4, I_5, I_6), \tag{3.6}$$

the current approach simplifies the model by retaining only the first term. This simplification reverts back to the classical Boussinesq eddy-viscosity model while preserving the functional form derived from Equation 3.6. The main motivation for this simplification is to reduce the model's complexity, enabling efficient training and evaluation. However, it is important to note that future advancements may involve the inclusion of additional terms to extend beyond the eddy-viscosity model.

In essence, the investigated model is an eddy-viscosity model given by

$$\nu_t = f(I_1, I_2, I_3, I_4, I_5, I_6; \theta), \tag{3.7}$$

where the eddy viscosity ν_t is a function of the inputs $I_1, I_2, I_3, I_4, I_5, I_6$ through the functional form $f(\cdot)$. The specific form of $f(\cdot)$ is given by the predictor and also depends on the flow type determined by the classifier, and additional parameters θ may also vary across different flow regions, which will be specified later. The adoption of this formulation inherently satisfies the requirement of invariance (Requirement (VI)). As the architecture of the model has been introduced in the previous chapter, we will focus on the inputs and outputs being used and the normalization of data in the forthcoming sections.

3.4.1   Classifier

The classification of a point in the flow domain is a two-step process. Initially, the flow is classified as either laminar or turbulent. Subsequently, in the case of turbulent flow, it undergoes further classification into three distinct categories: zero pressure gradient, mild adverse pressure gradient (APG), or separated flow. A visual representation of this workflow can be found in Figure 3-2.

The classifier's generated labels play a crucial role in determining the appropriate functional form of the eddy viscosity model to be applied. Specifically, the local label guides the selection of the neural network to which the inputs are directed. The formulation of these neural networks will be introduced soon in the next section.

Finally, it needs to be emphasized that the classifier is only used for the first grid points close to the wall. Points far from the wall share the same model regardless of the flow type. Such implementation comes first from the fact that for coarsely resolved WMLES, flow of different types share similar characteristics far from the wall. Also, if each flow type has its own model also far from the wall, the number of neural networks to be trained will be nearly doubled compared to the current version. In light of these factors, and considering that there is minimal loss in performance,
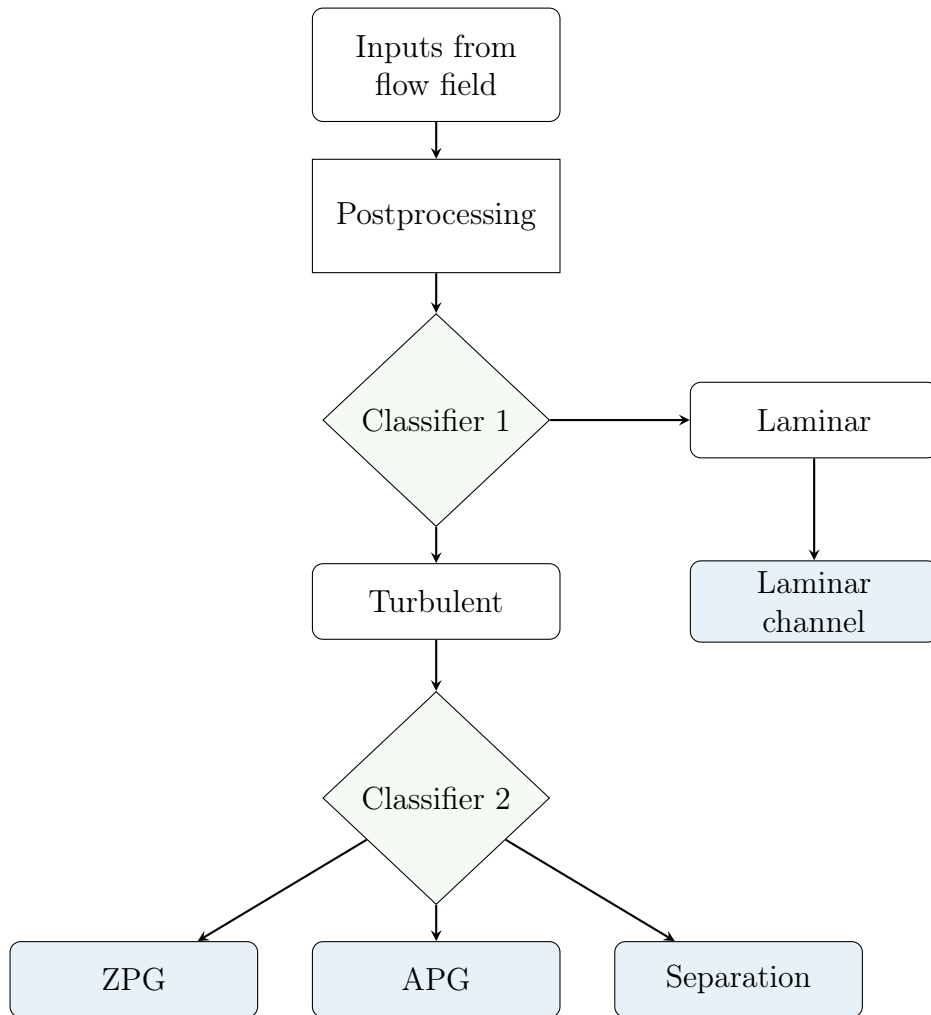
Figure 3-2: Workflow for two sequential classifiers. The first classifier determines whether the flow is laminar or turbulent. The second classifier determines the type of the turbulent flow. Light blue boxes indicate possible output labels from classifiers.

a decision has been made to employ a single model for all points far from the wall. However, for grid points near the wall, where the flow type significantly influences the prediction of both the eddy viscosity and the wall shear stress, a customized ANN is employed for each flow type.

3.4.2 Predictor

Two distinct types of ANNs are used for the predictors. The first type is used for the outer region. As mentioned in the Section 3.4.1, this ANN is universal among all the flow types. The second one is known as the near-wall predictor. It is employed for both the first grid points and the estimation of the eddy viscosity at the wall. The eddy viscosity at the wall, in turn, is utilized for predicting the wall shear stress. We follow the formulation from Bae et al. [49] and use a non-slip boundary condition augmented by an eddy viscosity at the wall

$$\nu_t|_w = \left(\frac{\partial \bar{u}}{\partial y}\right)\bigg|_w^{-1} \frac{\tau_w}{\rho} - \nu. \tag{3.8}$$

Figure 3-3 presents a summarized depiction of the two types of ANNs. These ANNs also differ in terms of their inputs and normalization procedures, which will be further discussed in the subsequent paragraphs.

3.4.2.1 Outer region

Aside from baseline inputs described in Equation 3.7, ANN for the outer regions takes as extra inputs Δ and ν. The grid size Δ is defined differently depending on the type of grid employed. In Cartesian grids, it is calculated as $\sqrt{\Delta x^2 + \Delta y^2 + \Delta z^2}$, while in control volumes of the charLES solver, it is defined as $V^{1/3}$, where V represents the volume of the grid.

Effects of two normalization strategies — a viscous scaling with ν and Δ and an inviscid scaling with $|S|$ and Δ — are tested and shown in Figure 3-4. It shows that data from different Reynolds numbers and grid sizes collapse better using the inviscid scaling.

41
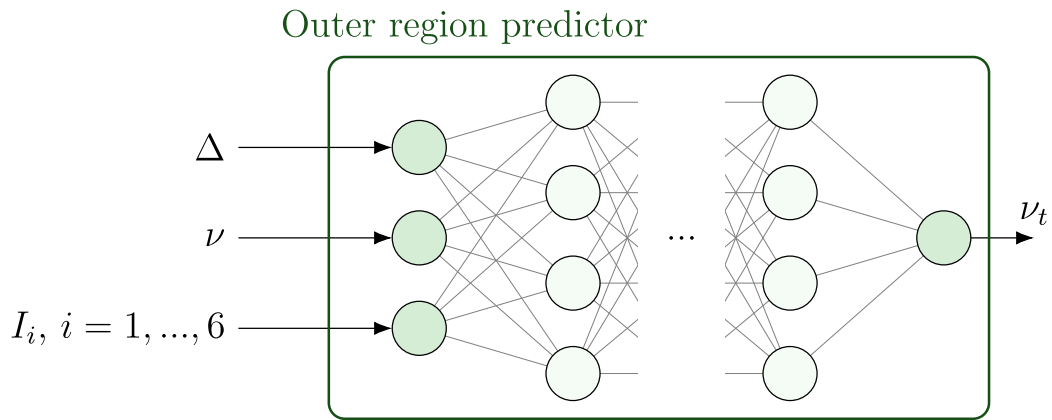
(a) The schematic of predictors used for the outer region.
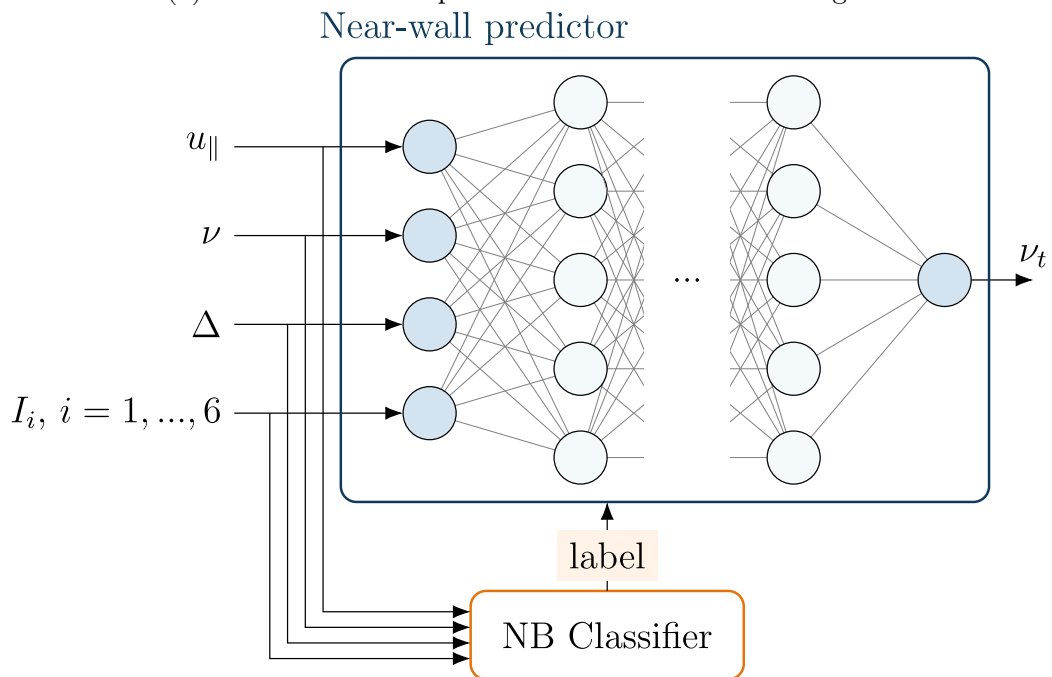
(b) The schematic of predictors used for near-wall region.

Figure 3-3: Schematics of two types of predictors. The predictor for the outer region is an ANN. The predictor for the near-wall region consists of an ANN and a classifier. The near-wall region predictor can be used to predict the eddy viscosity needed for the grid points close to the wall as well as the eddy viscosity at the wall required for the wall shear stress prediction.
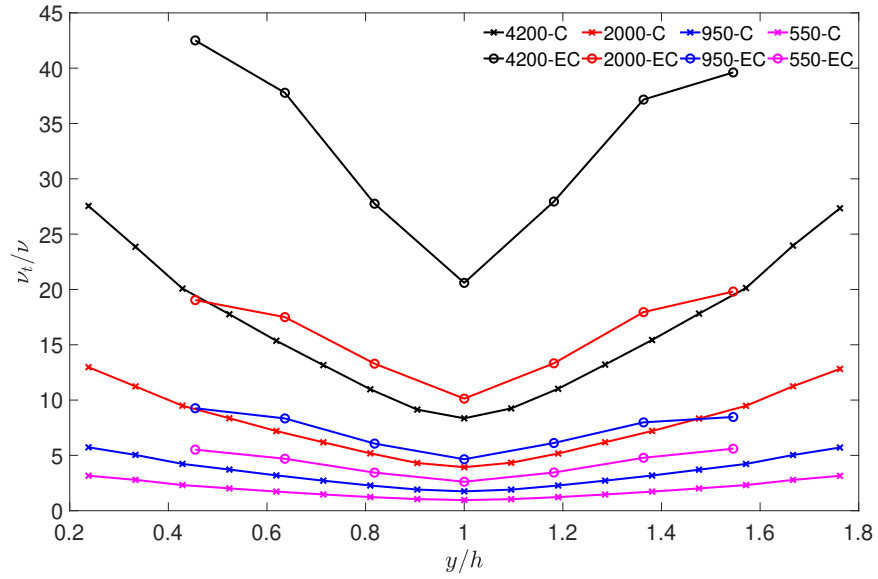
(a) Viscous Scaling
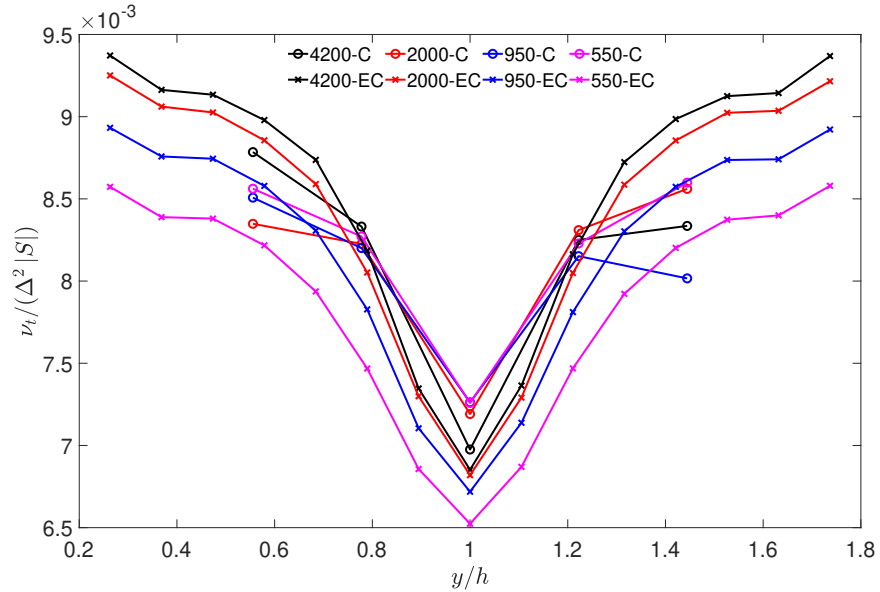
(b) Inviscid Scaling

Figure 3-4: Mean eddy viscosity at different channel height normalized by (a) a viscous scaling ν and Δ and (b) an inviscid scaling $|S|$ and Δ. Different curves correspond to cases with different Reynolds numbers and grid sizes (the format of names in legends is Re-Grid size).

In practice, a semi-viscous scaling approach, involving the quantities $(\sqrt{2\bar{S}_{ij}\bar{S}_{ij}}\nu)^{1/2}$ and Δ, has been found to yield the best generalization performance and is therefore employed.

3.4.2.2   Near wall

Compared to their outer-region counterpart, near-wall predictors take one extra input, i.e. the relative wall-parallel velocity $u_{\parallel}$. It can be computed as

$$u_{\parallel} = (\vec{u} - \vec{u} \cdot \vec{n}) - \vec{u}_w. \tag{3.9}$$

where $\vec{u}$ is the local velocity vector, $\vec{n}$ is the normal vector of the boundary and $\vec{u}_w$ is the velocity of the wall of interest. Both the inputs and outputs of the near-wall predictors are normalized using the viscous scaling approach, which involves the quantities ν and Δ.

3.5   Data Generation

The previous chapter briefly mentioned the distinction between the learning environment and the injection environment, as well as the potential errors arising from this discrepancy. However, the existing literature has not extensively addressed this issue. In this section, we propose a data generation method that tackles the problem of numerical errors. These errors are of particular concern in our case, where the grid size is coarse, and the numerical error can be comparable to other sources of error.

In contrast to traditional data generation methods that rely on filtered high-fidelity data obtained from DNS or wall-resolved LES, we adopt a different approach. Our data generation process involves carrying out WMLES simulations with an exact-for-the-mean eddy-viscosity and wall model, referred to as ESGSW. By using this method, we aim to mitigate numerical errors by utilizing training data consistent with the numerical schemes of the solver.

ESGSW consists of a conventional WMLES solver coupled with a controller. At

the end of each iteration, the controller adjusts the eddy-viscosity value to align with the mean velocity profile extracted from DNS simulations. This adjustment is accomplished by adding a correction term to the base eddy-viscosity model. In other words, the ESGSW model incorporates a corrective factor to refine the eddy-viscosity prediction

$$\nu_t^{ESGSW} = \nu_t^{SGS} + \Delta\nu_t^{SGS}. \tag{3.10}$$

In practice, ν_t^{SGS} can be the eddy viscosity predicted by any existing SGS models. In the current version of model, AMD model is selected to be the base model for BFM v0.1.0 and Vreman model for BFM v0.2.0. The specific choice of the base model is not expected to significantly impact the final results. However, it is worth noting that the controller may be more effective in correcting certain base models compared to others. This aspect can be explored further in future research as the model matures. In the following section, we discuss the process of obtaining the correction term $\Delta\nu_t^{SGS}$.

3.5.1 Controlling strategy

The control methods employed in two versions of BFM differ due to a combination of factors. Firstly, the variations in the control methods arise from the distinct numerical solvers used in each version. Secondly, the intention behind introducing new control methods is to enhance the effectiveness of the control process.

3.5.1.1 BFM v0.1.0

In the first version of BFM, a linear controller is employed to perform on-the-fly correction of the eddy viscosity. The correction term is determined by ensuring that the additional shear stress $\partial(2\Delta\nu^{SGS}\bar{S}_{ij})/\partial x_j$ assists in aligning the mean instantaneous streamwise velocity profile $\langle u \rangle_{xz}(y)$ with the corresponding profile obtained from DNS, denoted as $\langle u^{\text{DNS}} \rangle_{xzt}(y)$. An example showing the effect of the controller is Figure 3-5. While this controller yields reasonable results for channel flows with negligible to mild pressure gradients, its performance is not as satisfactory for flows characterized by strong pressure gradients. One possible reason for this disparity is

45

that the controller lacks the capability to effectively correct the original base SGS models, particularly in scenarios involving strong pressure gradients. Nonetheless, even in such cases, improvements are observed compared to the baseline model. The corrected models obtained through this process are subsequently utilized as inputs for the neural networks. The feasibility of this approach in this version of BFM is attributed to the structured Cartesian grid's utilization, which enables straightforward evaluation at each height along the wall-normal direction.
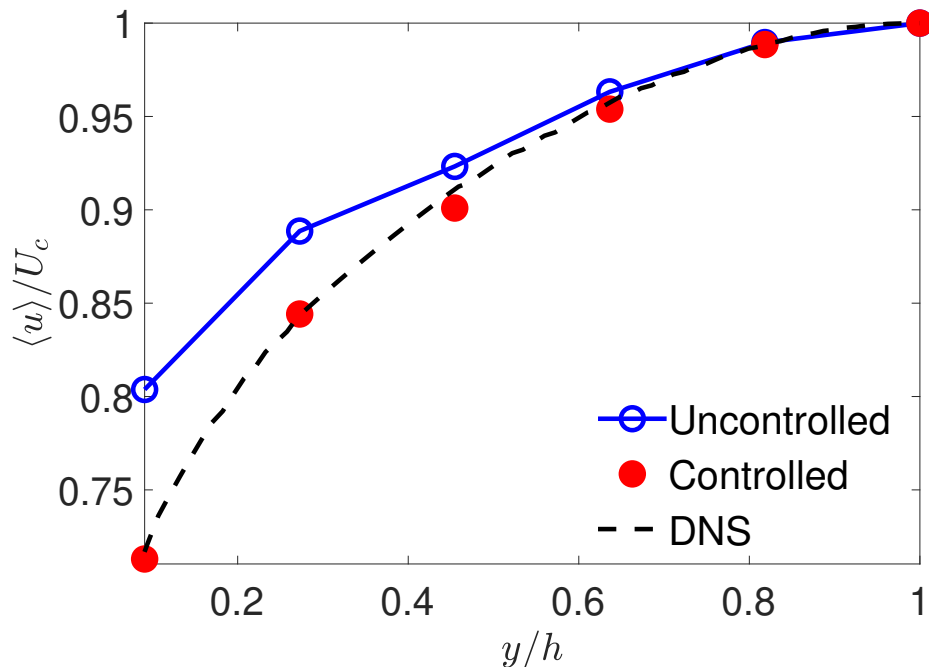
Figure 3-5: The effect of the linear controller on the mean streamwise velocity profile for turbulent channel flow with zero pressre gradient at $Re_\tau = 950$. U_c is the centerline velocity.

3.5.1.2   BFM v0.2.0

For BFM v0.2.0, a more advanced controlling strategy is adopted to systematically find the correction term. The correction is reformulated as

$$\nu_t(x, y, z, t) = \nu_t^{SGS}(x, y, z, t)k(y), \tag{3.11}$$

46

where the correction factors $k(y)$ are solely dependent on the wall-normal coordinate y. The task is then framed as an optimization problem:

$$\arg\min_{k(y)} \quad \int \left| \langle u^{\text{DNS}} \rangle_{xzt}(y) - \langle u \rangle_{xz}(y) \right|^2 dy. \tag{3.12}$$

To solve this problem, a Bayesian Global Optimization algorithm is employed [50]. The steps followed to solve the problem are as follows:

1. Initialize the control factor $k(y)$ with an initial guess.

2. A WMLES is run for a fixed wall shear stress $\tau_w = \tau_w^{DNS}$, where τ_w^{DNS} comes from the DNS data.

3. Evaluate the cost function, which quantifies the discrepancy between the DNS-based mean streamwise velocity profile $\langle u^{\text{DNS}} \rangle_{xzt}(y)$ and the computed mean streamwise velocity profile $\langle u \rangle_{xz}(y)$.

4. Run simulation until the steady state is reached.

5. Evaluate the cost function required for the optimization problem in Equation 3.12.

6. Update the control factor $k(y)$ using the Bayesian Global Optimization algorithm to minimize the cost function.

7. Steps 2-6 are repeated until convergence is achieved or a predetermined stopping criterion is satisfied.

The convergence criteria for turbulent channel flows is

$$\frac{\left| \langle u^{\text{DNS}} \rangle_{xzt}(y) - \langle u \rangle_{xz}(y) \right|}{\langle u^{\text{DNS}} \rangle_{xzt}(y)} < 0.03. \tag{3.13}$$

The criteria above is too stringent a criteria for PC cases close to separation as $\langle u^{\text{DNS}} \rangle_{xzt}(y)$ approaches zero. Therefore, an alternative criteria is enforced for PC cases:

$$\frac{\left| \langle u^{\text{DNS}} \rangle_{xzt}(y) - \langle u \rangle_{xz}(y) \right|}{u_\tau} < 0.02. \tag{3.14}$$

It is easier to achieve as the denominator is a constant and will not approach zero as the control factor $k(y)$ is updated.

3.5.2   Data selection

After the data generation process, a subset of the generated data needs to be selected for training the neural networks. In ZPG case, the entire flow field from 10 randomly chosen instantaneous snapshots from each case, obtained after reaching a statistically-steady state, is utilized for training the neural networks. However, for PC cases, only the lower half of the flow field is used for training purposes as they are more relevant to the flow physics for separation. For laminar flow, synthetic data for $Re_\tau = 5 - 150$ are generated from analytical solutions for training.

Table 3.1 presents an overview of the cases utilized for training neural networks. The ZPG cases cover a range of friction Reynolds numbers (Re_τ) up to 10,000, which represents the highest achieved Reynolds number in DNS. Additionally, there are two or three cases with different adverse pressure gradients included for BFM v0.1.0 and BFM v0.2.0, respectively. The selection of training data is tailored to the specific versions of BFM targeted for different solvers, using the aforementioned data generation process.

Although in theory, it is possible to obtain additional data from different setups, the practical application of the data generation process presents challenges. For instance, BFM v0.1.0 excludes data from PC cases with strong adverse pressure gradients after separation due to the failure of the naive controller to converge. In contrast, BFM v0.2.0 benefits from the improved controller, enabling the inclusion of such cases. However, the convergence time required for training is still considerable, limiting the inclusion of even more cases. Consequently, devising a more efficient and effective data generation strategy remains an open problem for future exploration.

It is also noteworthy that the data generation process only relies on obtaining the "true" mean profile, which allows for the possibility of utilizing experimental data rather than being restricted to existing DNS databases. For instance, experimental data obtained from atmospheric boundary layers or Superpipes, with frictional

Case	Re_τ	Δ_y/h	Version	Solver	DNS	Re_P
550-EC	547	0.2	v0.1.0	FD	Del Alamo et al.[51]	N/A
950-EC	943	0.2	v0.1.0	FD	Del Alamo et al.[51]	N/A
2000-EC	2003	0.2	v0.1.0	FD	Hoyas et al.[52]	N/A
4200-EC	4179	0.2	v0.1.0	FD	Lozano-Duran et al.[53]	N/A
550-C-c	0.547	0.1	v0.2.0	charLES	Del Alamo et al.[51]	N/A
950-C-c	943	0.1	v0.2.0	charLES	Del Alamo et al.[51]	N/A
2000-C-c	2003	0.1	v0.2.0	charLES	Hoyas et al.[52]	N/A
4200-C-c	4179	0.1	v0.2.0	charLES	Lozano-Duran et al.[53]	N/A
10000-C-c	10000	0.1	v0.2.0	charLES	Hoyas et al.[54]	N/A
550-EC-c	547	0.2	v0.2.0	charLES	Del Alamo et al.[51]	N/A
950-EC-c	943	0.2	v0.2.0	charLES	Del Alamo et al.[51]	N/A
2000-EC-c	2003	0.2	v0.2.0	charLES	Hoyas et al.[52]	N/A
4200-EC-c	4179	0.2	v0.2.0	charLES	Lozano-Duran et al.[53]	N/A
10000-EC-c	10000	0.2	v0.2.0	charLES	Hoyas et al.[54]	N/A
PC0	7	0.1	v0.1.0	FD	In-house	680
PC2	264	0.1	v0.1.0	FD	In-house	340
PCr	264	0.1	v0.2.0	charLES	In-house	962
PCs	7	0.1	v0.2.0	charLES	In-house	680
PCm	264	0.1	v0.2.0	charLES	In-house	340
Laminar	5-150	0.1	v0.1.0	N/A	N/A	N/A

Table 3.1: Cases selected to generate training data for BFM v0.1.0 and v0.2.0. The name of turbulent channel flow with zero pressure gradient cases consists of friction Reynolds number, the grid size (C for coarse; EC for extra coarse) and the solver (c for charLES; none for the in-house code) connected by hyphens. For PC cases, PCr, PCs and PCm stand for flow reversal, separation and mild adverse pressure gradient, respectively. They are run by charLES. PC with numbers are PC cases run by the in-house code with different degrees of adverse pressure gradients. Laminar cases are synthetic data generated from analytical solutions. "Version" column shows the version of BFMS where the case is used for training. "Solver" column refers to the solver used to generate the training data. "DNS" column shows the source of DNS mean profile, either from turbulence database or in-house DNS simulations. Re_P is the pressure gradient-based Reynolds number defined in Equation 3.2.
.

Reynolds numbers as high as 628,000, can be incorporated into our model [55]. This flexibility will be leveraged in the future for the extensibility and application of our model to even higher Reynolds number.

3.6 Neural Network Parameters

The mean squared error (MSE) is employed as the loss function, and the Rectified Linear Unit (ReLU) serves as the activation function. In BFM v0.1.0, all neural networks are fixed to have six layers, with each layer containing 40 neurons. However, for BFM v0.2.0, extensive experimentation was conducted to determine the optimal architecture. The final architecture adopted consists of six layers with 40 neurons for the outer-region predictor, ten layers with 16 neurons for the near-wall SGS predictor, and eight layers with the following number of neurons in each layer: [7, 8, 8, 8, 7, 6, 5, 3] for the wall shear stress predictor.

3.7 Training

The ANNs were trained using a scaled conjugate gradient backpropagation method by randomly partitioning training data into three groups, the training set (70% of the data), validation set (15% of the data) and test set (15% of the data). The training was stopped when the MSE of either the validation set or training set ceased to decrease, in order to achieve a balance between optimal performance and generalizability.

Chapter 4

Results

In this section, we present results obtained using the BFMs. First, we will examine the performance of the classifier. The accuracy and reliability of the classifier will be evaluated to ensure its effectiveness in distinguishing between different flow types. Following the evaluation of the classifier, we will proceed with conducting *a posteriori* tests using the BFMs. These tests will encompass canonical cases, including laminar channel flow, turbulent channel flow, turbulent Poiseuille-Couette flow, as well as more complex cases including CRM-HL and a Gaussian bump. The results are compared with reference data from the literature.

4.1 Classifier

The performance of the classifier is of utmost importance, as misclassification can lead to significant errors in the results. The accurate classification of flow types is crucial for guiding the predictions of the BFMs and ensuring reliable and physically meaningful results. For instance, misclassifying a wall-adjacent grid from a separated flow as ZPG channel flow could result in a severe overestimation of the wall shear stress. Such errors can propagate throughout the simulation and lead to inaccurate and unreliable predictions for various flow parameters and quantities of interest. Figure 3-2 illustrates the sequential flow of the two classifiers used to classify the flow into four categories. The first classifier is a binary classifier responsible for distinguishing

between laminar and turbulent flow. This initial classification task benefits from the relatively clear distinction between laminar and turbulent flow, allowing for accurate classification based on local flow information. The performance of the first classifier is excellent, achieving a one hundred percent accuracy for all the test cases. This indicates that the classifier effectively identifies and distinguishes between laminar and turbulent flow, solely utilizing the local flow characteristics.

The classification task performed by the second classifier, distinguishing between ZPG, APG, and separated flow, is more challenging compared to the laminar-turbulent classification. The performance of the second classifier is summarized in the confusion matrix shown in Figure 4-1. In the matrix, the labels "C", "A" and "S" represent ZPG flow, APG flow and separated flow, respectively. The confusion matrix provides an overview of the classifier's performance, indicating the percentage of samples from the true class that are correctly classified into the predicted class. Despite the increased complexity of the classification task, the second classifier demonstrates reasonable performance, with accuracy rates higher than 75% for all classes.

Figure 4-1: Performace of the classifier. "C" stands for ZPG flow, "A" for APG flow and "S" for separated flow.

To assess the potential loss of model performance due to misclassification, the sub-

sequent sections will include results obtained with a so-called "perfect" classifier. The "perfect" classifier is achieved by effectively disabling the classifier, always predicting the correct class. By comparing the results obtained with the "perfect" classifier to those with the actual classifier, we can gain insights into the extent to which misclassification may affect the model's predictions. This comparison allows for a clearer evaluation of the impact of the classifier's performance on the overall performance of the BFMs. Overall, while the classifier shows satisfactory performance for the test cases, its true effectiveness and contribution to the model's performance will be further evaluated in the subsequent *a posteriori* tests.

4.2 Validation in Canonical Cases

4.2.1 Laminar Channel Flow

The first *a posterior* test case is a laminar channel flow with a fixed centerline velocity. The simulation is started from a random flow field and the data are collected after transients. Figure 4-2 demonstrates that the BFM accurately predicts the laminar channel flow by correctly classifying all the points as laminar flow and subsequently providing accurate predictions. The BFM results align closely with the analytical solution for this test case. In terms of the wall shear stress, the analytical solution corresponds to a friction Reynolds number of $Re_\tau = 19.64$, while the BFM prediction yields a friction Reynolds number of $Re_\tau = 19.62$. This close agreement between the BFM prediction and the analytical solution validates the accuracy of both the classifier and the predictor components of the BFM.

4.2.2 Turbulent Channel Flow

Next, we analyze turbulent channel flow with zero pressure gradient. In addition to evaluating the trained cases on an extra coarse grid ($\Delta = 0.2h$), we also assess cases with a coarse grid ($\Delta = 0.1h$) that were not included in the training data. The focus is on two quantities: mean streamwise velocity and wall shear stress. The
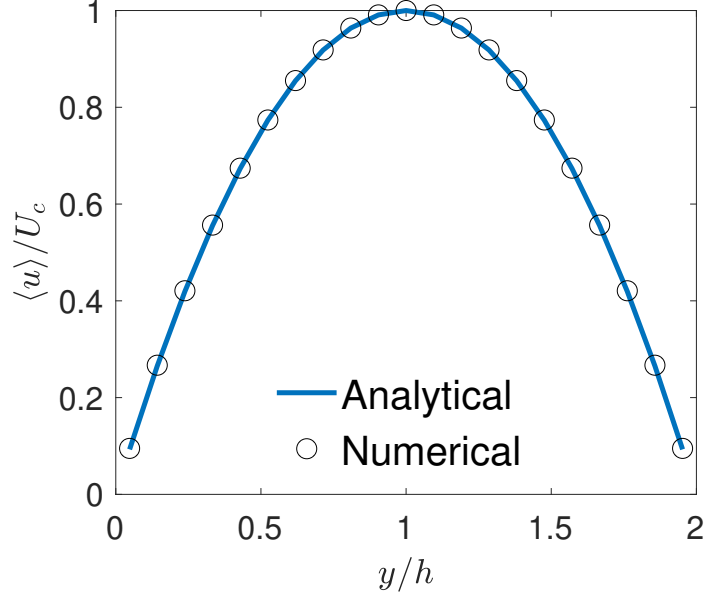
Figure 4-2: Mean streamwise velocity profile for laminar channel flow (U_c is the centerline velocity).

objective is to test the model's performance and also its generalizability to different grid configurations.

4.2.2.1 Wall shear stress

Case	Re_τ	DSM-EQWM	Vreman-EQWM	BFM	Trained
550-EC	547	587(7.3%)	578(5.7%)	**540(1.3%)**	✓
950-EC	943	1034(9.7%)	1002(6.3%)	**929(1.5%)**	✓
2000-EC	2003	2228(11.2%)	2157(7.7%)	**1976(1.3%)**	✓
4200-EC	4179	4641(11.1%)	4474(7.1%)	**4179(0.0%)**	✓
550-C	547	552(0.9%)	**545(0.4%)**	537(1.8%)	✗
950-C	943	973(3.2%)	**944(0.1%)**	906(3.9%)	✗
2000-c	2003	2137(6.7%)	2050(2.3%)	**1988(0.7%)**	✗
4200-C	4179	4502(7.7%)	**4286(2.6%)**	4006(4.1%)	✗

Table 4.1: Friction Reynolds numbers predicted by different SGS and wall models. Re_τ are the benchmark values from DNS. The "Trained" column shows whether the case has been used for training. Definitions of trained cases can be found in Table 3.1. Numbers in parentheses are the relative errors defined by $|(Re_{\tau,\text{pred}} - Re_\tau)/Re_\tau|$.

Table 4.1 provides a summary of the wall shear stress results for turbulent channel

flow with zero pressure gradient. The performance of the BFM is evaluated for different grid resolutions, including the trained grid resolution and finer grids. For the trained grid resolution, the BFM exhibits the highest level of performance, surpassing other models by a significant margin. It demonstrates good accuracy in predicting the wall shear stress with coarse grids. For the untrained finer grids, the performance of the BFM slightly deteriorates, while the accuracy of the Vreman-EQWM model improves significantly. Despite the small deterioration, the relative error of the BFM remains acceptable, outperforming the prediction from the DSM-EQWM model.

4.2.2.2   Mean Velocity Profile

Extra Coarse Grid ($\Delta = 0.2h$)   Figure 4-3 presents a comparison of the results obtained from WMLES using all three models with the reference DNS data. The comparison is conducted for four different Reynolds numbers.The results demonstrate that the BFM outperforms the other models for all four Reynolds numbers examined. This outcome was expected since the BFM was trained on the same grid resolution, whereas the other models are known to perform poorly on very coarse grids.

Coarse Grid ($\Delta = 0.1h$)   Figure 4-4 displays the results obtained from WMLES for a coarse grid ($\Delta = 0.1h$). In comparison to the results obtained on the trained extra coarse grid (Figure 4-3), it is observed that both the DSM-EQWM and Vreman-EQWM models show improvements in their performance. On the other hand, the BFM's performance slightly worsens. This outcome is anticipated, as the BFM was not trained on this specific grid resolution. Furthermore, it is important to note that WMLES exhibits a well-known non-monotonic convergence behavior when the grid is refined. Therefore, the observed behavior may also be attributed, in part, to this effect.
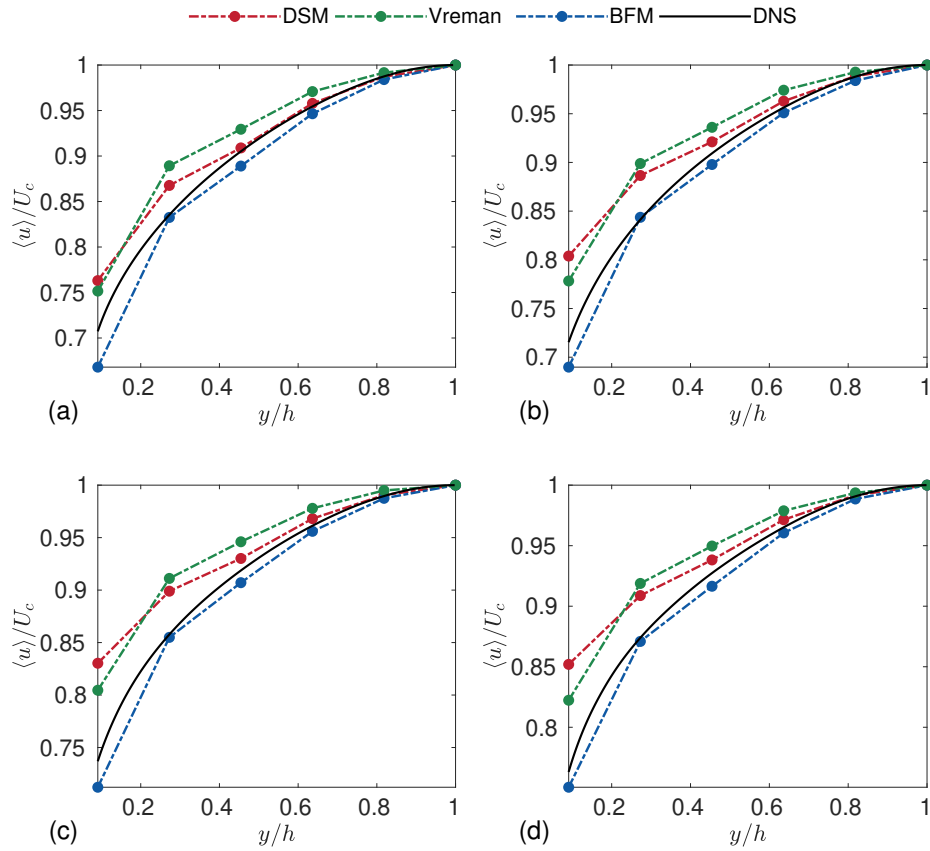
Figure 4-3: Mean streamwise velocity predictions for turbulent channel flow using an extra coarse grid ($\Delta = 0.2h$). (a) $Re_\tau \approx 550$, (b) $Re_\tau \approx 950$, (c) $Re_\tau \approx 2000$ and (d) $Re_\tau \approx 4200$.
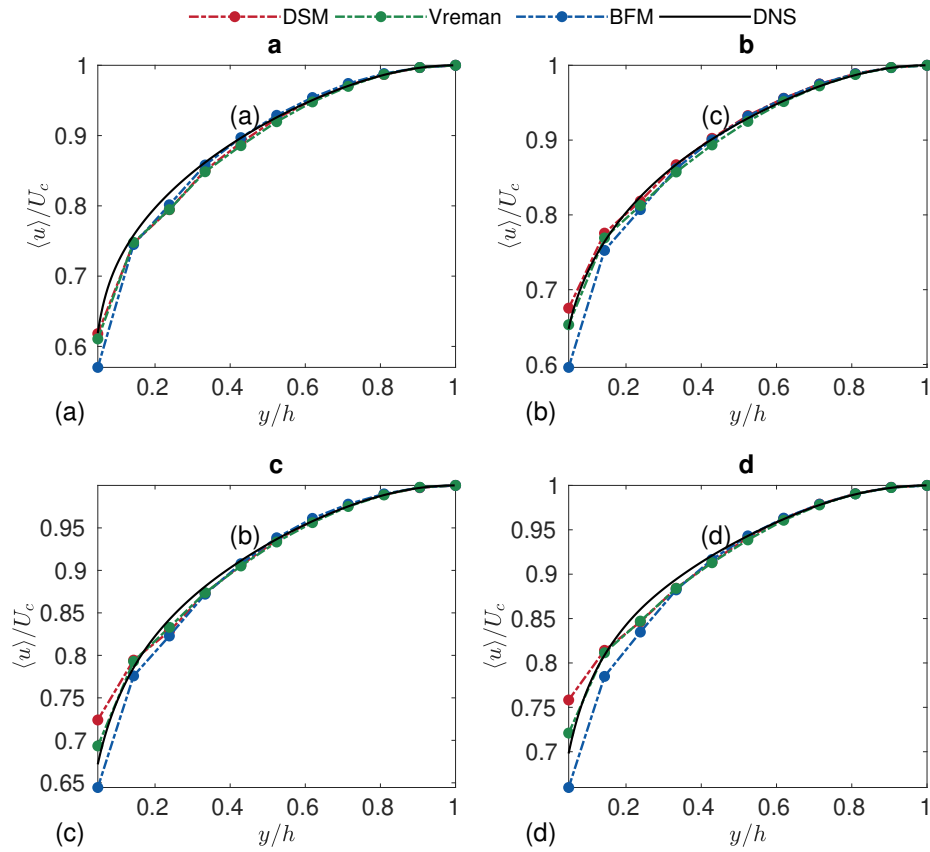
Figure 4-4: Mean streamwise velocity for turbulent channel flow using a coarse grid ($\Delta = 0.1h$). (a) $Re_\tau \approx 550$, (b) $Re_\tau \approx 950$, (c) $Re_\tau \approx 2000$ and (d) $Re_\tau \approx 4200$.

4.2.3 Turbulent Poiseuille-Couette Flow

The final canonical case under examination is turbulent Poiseuille-Couette flow with varying adverse pressure gradients. In addition to assessing the trained cases, we also investigate the model's generalizability by examining cases with adverse pressure gradients that were not included in the training data. This analysis enables us to evaluate the model's ability to extend its predictions to unseen flow configurations.

4.2.3.1 Wall shear stress

Table 4.2 provides a summary of the results for turbulent Poiseuille-Couette flow with different adverse pressure gradients.

Case	Re_τ	DSM-EQWM	Vreman-EQWM	BFM	Trained	Re_P
PC0	7	76(1014%)	68(871%)	**33(371%)**	✓	680
PC1	194	164(15.5%)	169(12.9%)	**172(11.3%)**	✗	480
PC2	264	225(14.8%)	221(16.3%)	**227(14.0%)**	✓	340

Table 4.2: Friction Reynolds numbers predicted by different SGS and wall models. Re_τ are the benchmark values from DNS. The "Trained" column shows whether the case has been used for training. Definitions of trained cases can be found in Table 3.1. Numbers in parentheses are the relative errors defined by $|(Re_{\tau,\text{pred}} - Re_\tau)/Re_\tau|$. Re_P is the pressured gradient-based Reynolds numbers defined in Eq 3.2.

The results demonstrate that, for both untrained and trained cases, BFM achieves the best performance. It is important to note that for the PC0 case, which is close to separation, the relative error appears large due to the near-zero denominator in the calculation. However, this does not indicate significant errors in the model's predictions.

4.2.3.2 Mean streamwise velocity profile

Figure 4-5 shows the mean streamwise profile obtained for turbulent Poiseuille-Couette flow with different adverse pressure gradients. Among the trained cases, namely PC0 (near separation) and PC2 (mild adverse pressure gradient), the BFM demonstrates superior predictive capabilities, outperforming the other models. However, for the
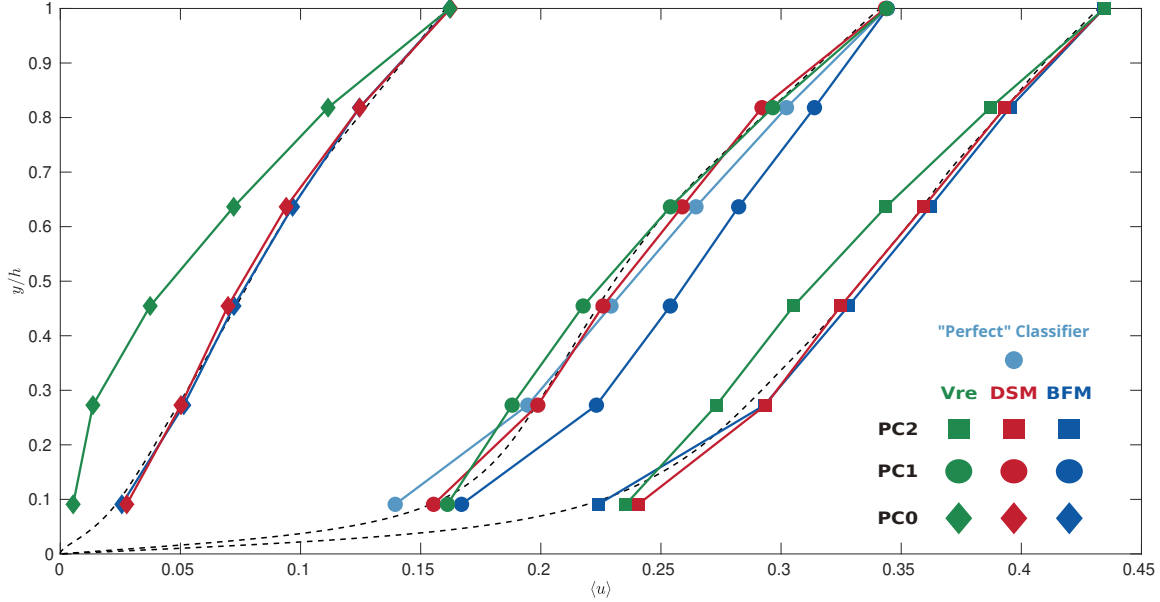
Figure 4-5: Mean streamwise velocity for Poiseuille-Couette flow. Three cases, PC0 (separation), PC1 (intermidiate APG) and PC2 (mild APG), are overlaid on the same plots.

untrained case PC1 (intermediate adverse pressure gradient), the BFM does not outperform the other two models. To investigate the source of the error, a "perfect" classifier, which always predicts the correct class, is utilized for the PC1 case. The *a posteriori* results obtained using the BFM with the "perfect" classifier are represented by the light blue line in Figure 4-5. It is observed that the "perfect" classifier significantly improves the prediction. Additionally, the corresponding friction Reynolds number is calculated to be 185 with a relative error of 4.6%, indicating a substantial improvement.

These findings confirm the importance of the classifier in determining the overall performance of the BFM. The error observed in the BFM's prediction for the PC1 case can be attributed to the classification error. This empirical evidence further supports the argument that the accuracy of the classifier is crucial for achieving accurate and reliable predictions with the BFM.

4.2.4 Conclusions

Throughout the examination of various canonical cases, the BFM consistently demonstrates improvements over other state-of-the-art models. This superiority is particularly pronounced when considering the coarsest grid resolutions. In the context of turbulent Poiseuille-Couette cases, it becomes evident that the accuracy of the BFM is strongly influenced by the performance of the classifier. Therefore, further enhancements and improvements to the classifier are crucial for achieving even better results in future applications.

4.3 Validation in Complex Cases

The two realistic test cases chosen for examination are the NASA Common Research Model High-lift (CRM-HL) and a Gaussian bump. These simulations are conducted using the flow solver charLES.

4.3.1 CRM-HL

The CRM-HL is tested in this section as a representative of realistic aircraft in high-lift configuration [56]. It is a geometrically complex aircraft that includes the bracketry associated with deployed flaps and slats as well as a flow-through nacelle mounted on the underside of the wing. It has been the new benchmark for high-lift computational aerodynamics in place of the the old one, JAXA Standard Model configuration by the Japanese Aerospace Exploration Agency (JAXA) [57]. Results shown in this section can also be found in [30].

4.3.1.1 Case Description and Computational Set-up

We focus on free air simulations. Experimental data used for comparison have been corrected to account for wind tunnel and side wall effects following the standard practice [58]. The experimental setup carried out by Evans et al. is shown in Figure 4-6 [59].
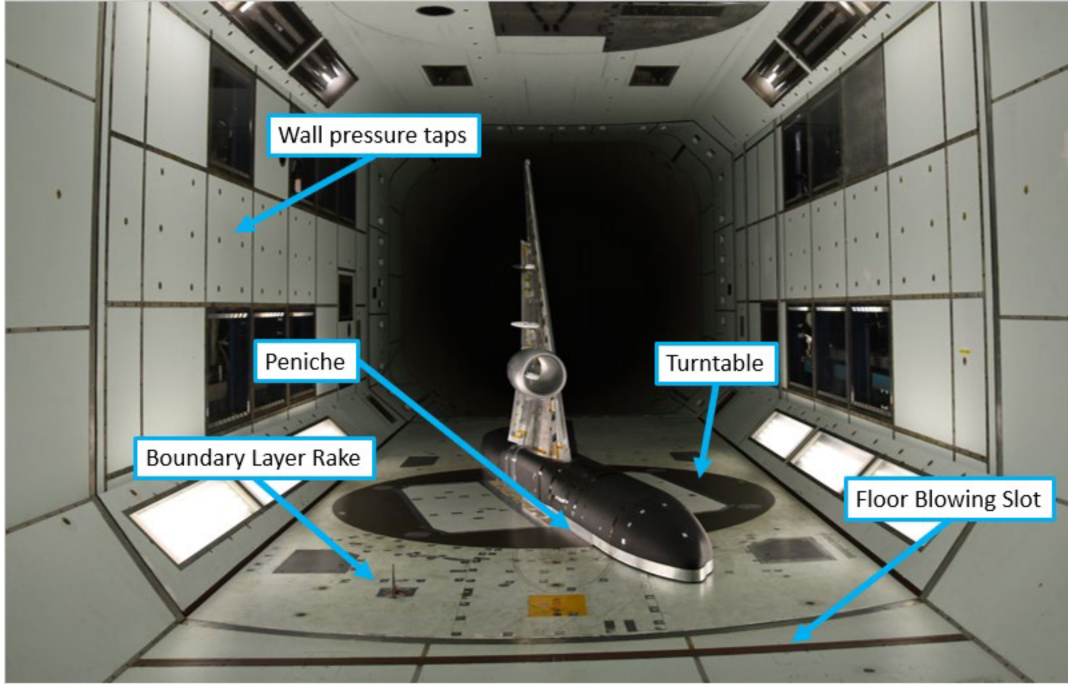
Figure 4-6: 10% NASA semi-span CRM-HL installed at the QinetiQ 5-Metre Low-Speed Wind Tunnel [59].

The Reynolds number based on the mean chord and freestream velocity is $Re_c = 5.49 \times 10^6$. The freestream Mach number is 0.20. We follow the computational setup from Goc et al. [58]. A semi-span aircraft geometry following the experimental setup is simulated and the symmetry plane is treated with free-slip and no penetration boundary conditions. A uniform plug flow is used as the inlet. A non-reflecting boundary condition with specified freestream pressure is imposed at the outlet [60]. For additional information regarding the gridding strategy and other technical details, readers are referred to the work by Goc et al. [58].

We perform simulations for two AoAs, $\alpha = 7.05°$ and $19.57°$, corresponding to a moderate AoA and a high AoA with maximum lift before stalling. The total number of grid points is 40 million and the number of grid points per boundary layer thickness ranges from zero to twenty. A slice of the grid is depicted in Figure 4-7.

One caveat for the current results is that it is run by BFM v0.1.0, which is trained in our in-house finite-difference solver. It also assumes a zero pressure gradient (ZPG)

condition and therefore turns off the classifier. In theory, it is not capable of compensating for the numerical error in charLES. In the future, we will apply the BFM v0.2.0, which is trained in charLES, to CRM-HL to achieve a better performance. Nonetheless, current results are still useful for us to understand the performance of BFMs in realistic cases.
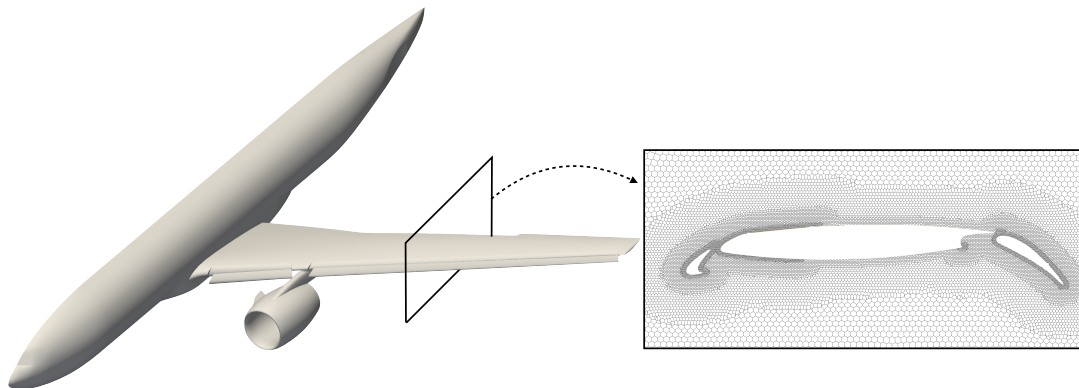
Figure 4-7: The cross-sectional view of high-quality hexagonal grids generated by Voronoi diagram-based approach for CRM-HL in charLES.

4.3.1.2 Results

We compare the lift (C_L), drag (C_D) and pitching moment (C_M) coefficients with experimental data and simulations from [58] using DSM with EQWM (labeled as DSM-EQWM) for two AoAs, 7.05° and 19.57°. Results are shown in Figure 4-8.

Moderate AoA ($\alpha = 7.05°$)   Both BFM and DSM-EQWM demonstrate high accuracy in predicting the quantities of interest, namely lift and drag coefficients. DSM-EQWM yields highly accurate results for these coefficients, which may suggest its superiority over BFM at first glance. However, a closer examination of the pressure distribution (see the following sections) reveals that the good prediction is a direct result of error cancellation. When analyzing the pitching moment coefficient, BFM outperforms DSM-EQWM in terms of accuracy.

(a) Lift coefficients

(b) Drag coefficients

(c) Pitching moment coefficients
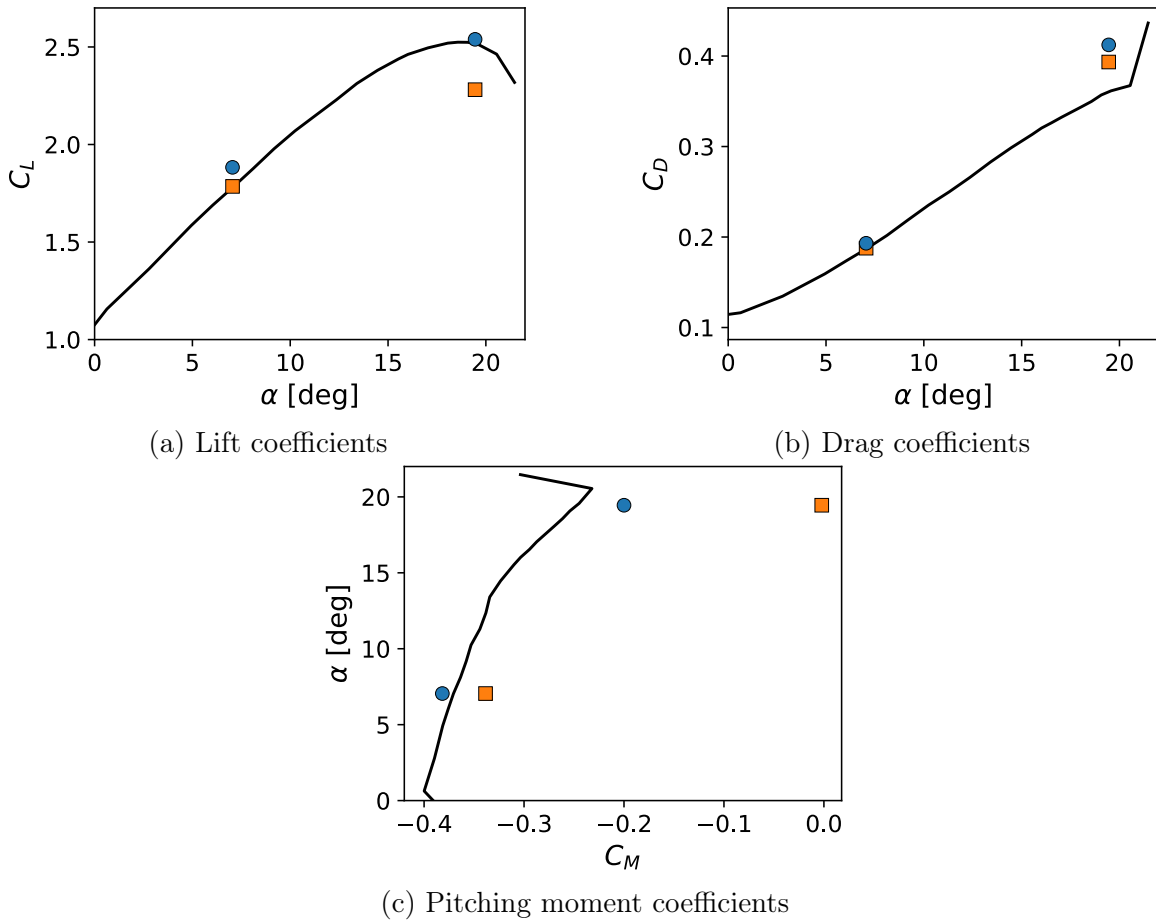
Figure 4-8: Lift (C_L), drag (C_D) and pitching moment (C_M) coefficients. The black lines denote experimental results, orange squares are for DSM-EQWM and blue circles are for BFM. Note that for (c), AoAs are plotted in the vertial axis different from the conventions used for (a) and (b).

High AoA ($\alpha = 19.57°$) DSM-EQWM underpredicts the lift coefficients, while BFM provides accurate predictions. As for the drag coefficients, both models tend to overpredict, but the result by DSM-EQWM is slightly closer to the experimental values. It is important to note that these observations are again subject to further investigation into the pressure distribution. Regarding the pitching moment coefficients, both models also tend to overpredict the quantity, but the results by BFM are closer to the experimental values compared to DSM-EQWM.

Pressure Distribution The accuracy of integrated quantities examined above does not give a complete picture of the performance of the model since it could well be a result of error cancellation. Further analysis of the local predictions, therefore, is crucial to gain a comprehensive understanding of the models' performance. In this study, the 82% spanwise section of the wing for $\alpha = 19.57°$ is examined, and the pressure coefficient distribution is analyzed (Figure 4-9).

The pressure coefficient distribution reveals that DSM-EQWM poorly predicts the spatial distribution of the pressure coefficient. Therefore, the accurate prediction of integrated quantities such as lift and drag coefficients is coincidental, most likely results of error cancellation when integrating the total forces. On the other hand, BFM accurately predicts the pressure distribution, indicating that its high accuracy in predicting lift and drag coefficients is physically more consistent. Consequently, BFM is expected to provide more reliable results for different AoAs. Finally, from the pressure coefficient distribution shown in Figure 4-9, it can be observed that BFM maintains the flow attached over a longer section of the wing compared to DSM-EQWM. This physical behavior explains the enhanced performance of BFM in accurately predicting the lift and drag coefficients.

4.3.1.3 Conclusions

In conclusion, our study demonstrates that BFM is a more robust and accurate model compared to DSM-EQWM for both AoAs considered. BFM represents an improvement over state-of-the-art WMLES models for realistic computational aerodynamics
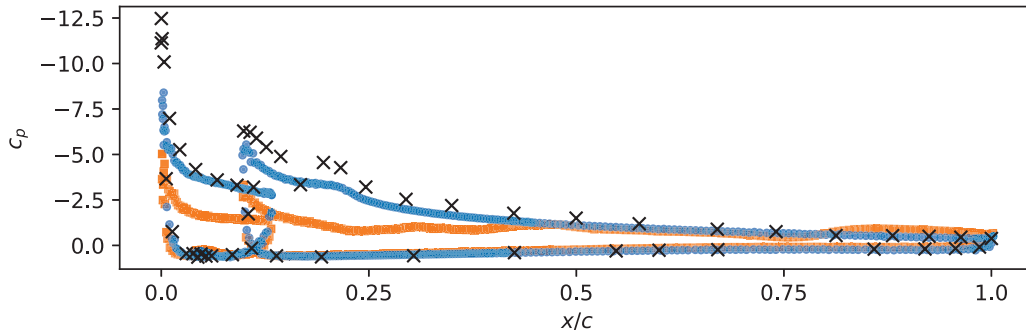
Figure 4-9: The pressure coefficient at the 82% spanwise section of the wing for $\alpha = 19.57°$. Black $\times$ represents experimental results, orange squares are for DSM-EQWM and blue circles are for BFM.

applications, even without compensating for numerical errors in the current implementation. The accurate prediction of lift and drag coefficients, as well as the pressure distribution on the wing, highlights the improved performance and flow physics representation achieved by BFM. Further development and refinement of BFM, including addressing numerical errors, have the potential to push it to the forefront of WMLES models for aerodynamic applications.

4.3.2 Gaussian Bump

The second case used to examine the model performance is a three-dimensional tapered bump, also known as the Gaussian bump. This case serves as an exemplary test for CFD models and methods, particularly for assessing their capability to handle boundary layers with separation and reattachment. Compared to the more complex CRM-HL case, which involves additional flow physics beyond separation and reattachment, the Gaussian bump provides a benchmark for isolating these features. Additionally, due to its simplicity, it has been extensively studied in the literature, with comparisons across various CFD methods with different fidelity. Recent CFD of the Gaussian bump include DNS by Uzun et al. [61], WMLES by Iyer et al. [62], Iyer et al. [63] and Agrawal et al. [64] with various grid sizes and models and RANS by Williams et al. [65]. The consensus from these studies is that new models are

needed to improve the accuracy of coarsely resolved simulations Therefore, a good performance on this test case would indicate that the BFM model is a step in the right direction.

For this test case, BFM v0.2.0 is employed. Since BFM v0.2.0 has been trained using data from charLES solver, it is expected to account for the numerical errors. To date, the classifier has not been implemented for this version. The addition of a classifier in the future will further improve the accuracy of the model. Results shown this section can also be found in [29, 66].

4.3.2.1 Case Description and Computational Setup

Three-dimensional simulations are carried out for flow over a Gaussian bump. The geometry of the bump is given by the analytical formula

$$z(x,y) = \frac{h_0}{2} \exp\left(-\left(\frac{x}{x_0}\right)^2\right)\left[1 + \text{erf}\left(\frac{\frac{L}{2} - 2y_0 - |y|}{y_0}\right)\right], \qquad (4.1)$$

where x, y and z are the streamwise, spanwise and vertical directions, respectively, L is the length of the bump, and the parameters $h_0 = 0.085L$, $x_0 = 0.195L$ and, $z_0 = 0.06L$ define the shape of the bump [65].

The three-dimensional field is shown in Figure 4-10, where the main flow direction is along the x axis (streamwise direction). Cross-sectional views are shown in Figure 4-11 and Figure 4-12.

The non-dimensional parameters that define the flow are the Reynolds number based on the bump length and the free-stream velocity (U_∞), $Re_L = U_\infty L/\nu$, where ν is the free-stream kinematic viscosity; and the Mach number, $M = U_\infty/a_\infty$, where a_∞ is the free-stream speed of sound.

Present simulations are performed at $Re_L = 3.4 \times 10^6$ and $M = 0.176$. These values are consistent with those reported in [65], where the pressure coefficient along the centerline was investigated. Additionally, the values are comparable to those studied in [67], where the friction coefficient and flow field were experimentally computed for $Re_L = 2 \times 10^6$ and $M = 0.2$. This allows for meaningful comparisons and assessments
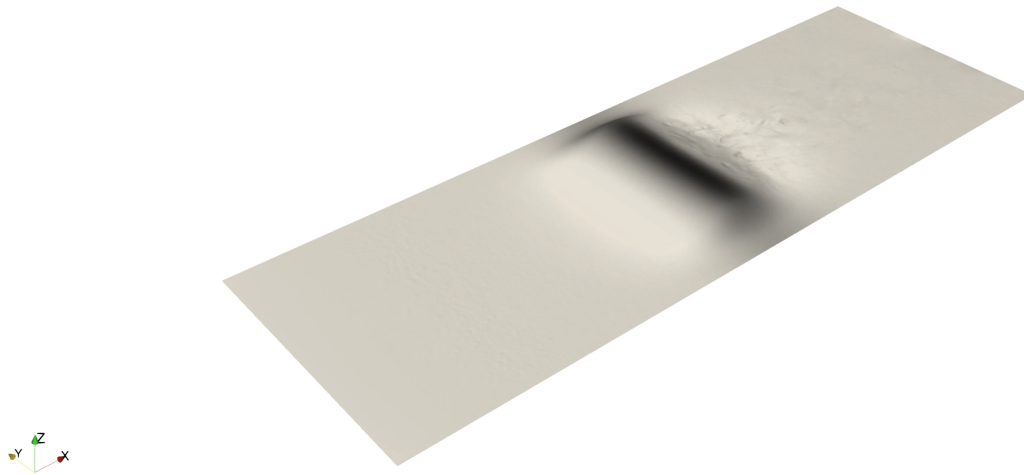
Figure 4-10: 3D view of the Gaussian bump computational field.
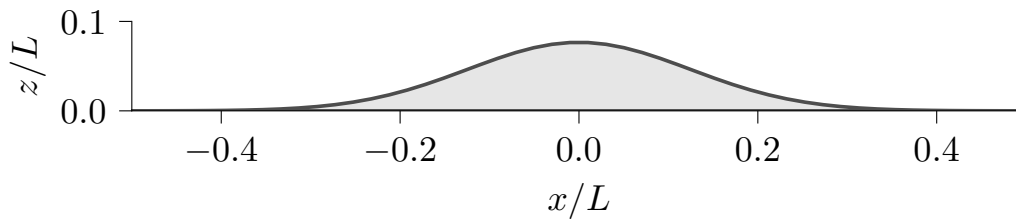
Figure 4-11: Cross-sectional view of the Gaussian bump at $y/L = 0$.
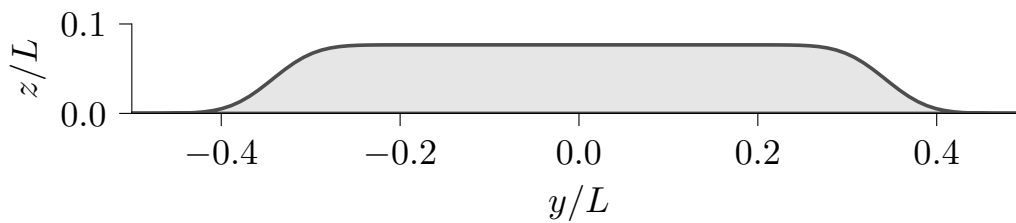
Figure 4-12: Cross-sectional view of the Gaussian bump at $x/L = 0$.

of the model's performance in a similar flow regime.

The computational domain is a rectangular prism that extends $\pm 1.5L$ in the streamwise direction, $\pm 0.5L$ in the spanwise direction and from $0L$ to $0.5L$ in the vertical direction. The lateral and top boundaries are free-slip, a constant uniform inflow is imposed at the inlet, and the non-reflecting characteristic boundary condition with constant pressure is applied at the outlet. These boundary conditions are consistent with those employed in previous studies such as [62] and [64].

Two grids with different sizes are considered: an extra coarse grid and a coarse one as shown in Figure 4-13a and Figure 4-13b, respectively. Each refinement level

(a)

(b)
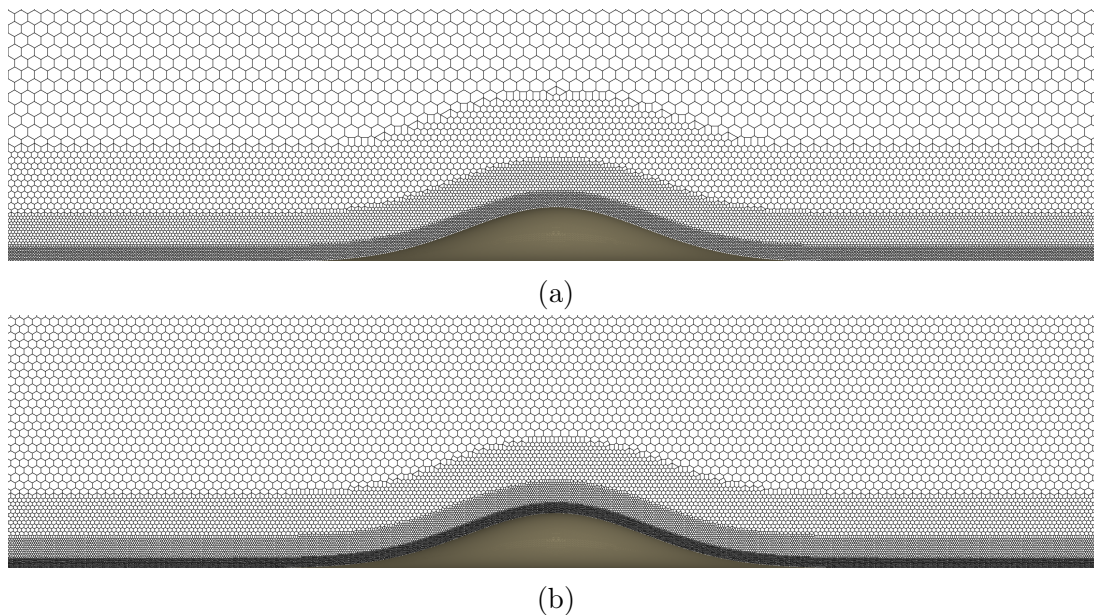
Figure 4-13: Grid structure in the $y/L = 0$ plane. (a) Extra coarse grid; (b) Coarse grid. Note that the pictures does not include the whole domain in the streamwise direction.

has roughly 10 control volumes along the wall-normal direction and the average size of each level is twice the size of the previous level. The grid size of the layer closer to the wall is the smallest and is referred to as $\Delta_{\min}$. For the extra coarse grid, $\Delta_{\min}/L$ (where L is the characteristic length of the domain) is approximately 2.2×10^{-3}. For the coarse grid, $\Delta_{\min}/L$ is approximately 1.4×10^{-3}. The latter grid size is similar to the coarse grid used in [64], hence the name "coarse grid". The grid size and number of elements for both grids are summarized in Table 4.3.

Mesh	$\Delta_{\min}/L$	N_{cv}
Extra coarse	2.2×10^{-3}	8.7×10^6
Coarse	1.4×10^{-3}	20.3×10^6

Table 4.3: Minimum grid size and number of control volumes, N_{cv}.

4.3.2.2 Results

We assess the performance of the BFM to predict average quantities of interest in the Gaussian bump. These quantities include the average wall pressure and friction coefficients, the location of the separation bubble, and the mean velocity profiles. The results are compared to those from Dynamic Smagorinksy model (DSM) with the equilibrium wall model (EQWM). In the following, we refer to this model as DSM-EQWM-X, where X is the grid: ExtraC(oarse) or C(oarse). All the quantities have been averaged for at least $30U_\infty/L$ convective time units after the initial transient has been discarded.

Wall pressure   The average pressure coefficients are defined as

$$C_p = \frac{p - p_\infty}{\frac{1}{2}\rho_\infty U_\infty^2}, \tag{4.2}$$

where p is the pressure averaged over time and p_∞ and ρ_∞ are the reference pressure and density. The results for all cases Figure 4-14a. The experimental results show that along the streamwise direction, there is first a favorable pressure gradient region for $x/L < 0$ followed by adverse pressure gradient region for $x/L > 0$. The mean separation point is at $x_s/L = 0.1$, represented by an inflection point. The reattachment happens on average at $x_r/L = 0.36$.

For the FPG region, all models predict the evolution of the pressure coefficients correctly regardless of the grid resolution. The APG region is more challenging to predict due to the separation. DSM-EQWM-ExtraC fails to predict the inflection point, leading to overprediction of C_p in the recirculation region. DSM-EQWM-C succeeds to capture the inflection point but the pressure inside the separation bubble is still overpredicted. For the BFM, the inflection point is captured for both

grid resolutions. While C_p in the second half of the separation bubble is accurately predicted, C_p in the first half remains constant and is overpredicted. BFM is also less sensitive to the change of grid size compared to DSM-EQWM.

Friction coefficients The prediction of the friction coefficient is shown in Fig. 4-14b. The experimental values show an abrupt increase of C_f in the FPG region towards the apex of the bump, where the friction coefficient reaches its maximum value. This is followed by a sudden drop in the APG, where $C_f < 0$ in the recirculation region. The trend of C_f in the FPG is consistent for all the models regardless of the grid resolution. Although none of the models is able to match the experimental results in the FPG region, it is interesting to note that BFM underpredicts the wall shear stress. This is expected as the building-blocks used for training BFM do not include cases with favorable pressure gradients. Also, note that the friction coefficient predicted by the DSM-EQWM-ExtraC for $x/L < -1$ is lower than the experimental value and the BFM predictions. This discrepancy is attributed to the fact that the flow is laminar for DSM-EQWM-ExtraC in that region, while BFM predicts a turbulent flow along x for the same grid resolution.

Case	x_s/L	x_r/L
Gray et al. [67]	0.10	0.36
DSM-EQWM-ExtraC	0.13	0.25
DSM-EQWM-C	0.09	0.31
BFM-ExtraC	0.13	0.36
BFM-C	0.10	0.36

Table 4.4: Location of mean separation point (x_s) and mean reattachment point (x_r) along the centerline for the different cases

Separation and Reattachment Points The mean separation point (x_s) and reattachment point (x_r) are defined as the streamwise locations where $C_f = 0$ in this study. Table 4.4 presents the mean separation and reattachment points along the centerline for the different cases. DSM-EQWM-ExtraC predicts larger friction coefficients than the experimental results for $x/L > 0$. As a result, the recirculation
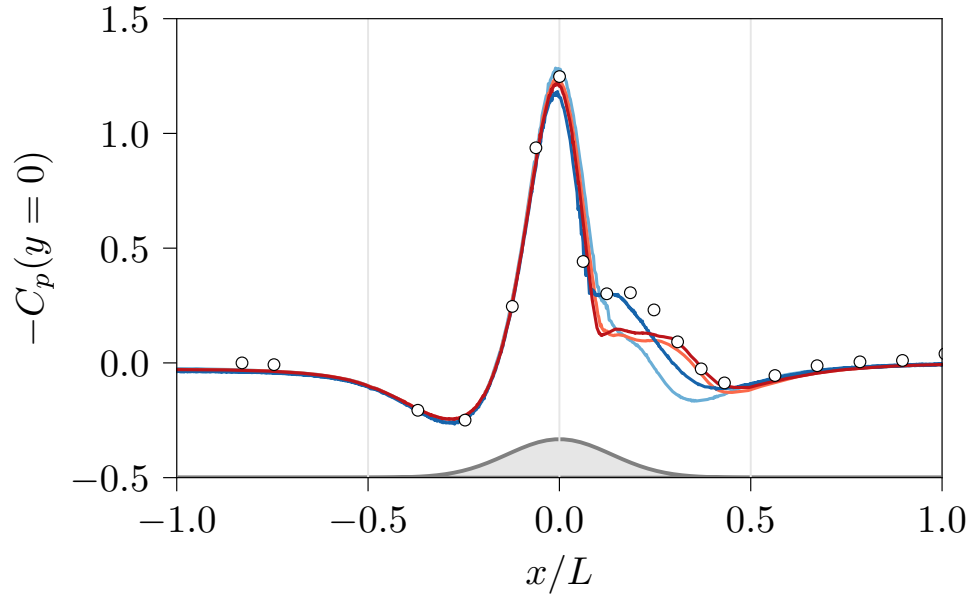
(a)
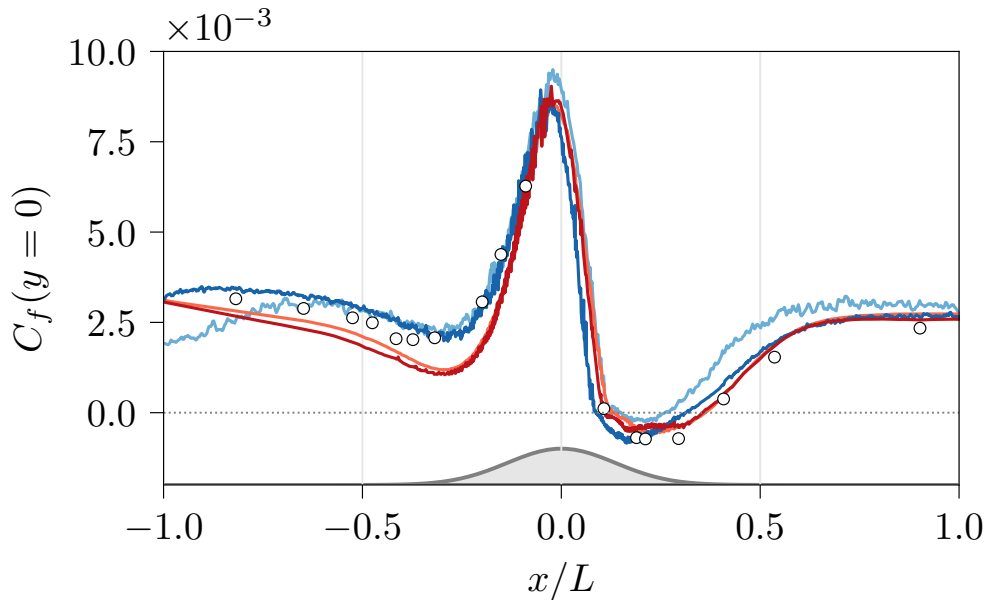
(b)

Figure 4-14: (a) Average pressure coefficients and (b) average friction coefficients over the bump surface at $y/L = 0$. Line colors correspond to (light blue) DSM-EQWM-ExtraC; (dark blue) DSM-EQWM-C; (light red) BFM-ExtraC; and (dark red) BFM-C cases. White circles in (a) correspond to experimental results from [65] at $Re_L = 3.41 \times 10^6$, $M = 0.17$, and (b) experimental results from [67] at $Re_L = 2 \times 10^6$, $M = 0.2$.

region is smaller and the onset of separation is delayed. DSM-EQWM-C, on the other hand, shows improved predictions of the separation point and a slightly larger separation bubble size ($0.22L$). However, the size of the bubble is still smaller than the experimental value ($0.26L$).

The performance of BFM-ExtraC in the APG region is superior to DSM-EQWM-ExtraC. Although the prediction of x_s is identical, BFM-ExtraC captures the exact location of reattachment, improving upon DSM-EQWM-C. Additionally, the values of C_f for $x/L > 0.1$ in BFM-ExtraC are closer to the experimental values. Although BFM-ExtraC slightly underpredicts the friction coefficient in the first half of the recirculation region, it matches the experimental values well for $x/L \gtrsim 0.23$. By increasing the grid resolution to BFM-C, the model is able to match the exact location of x_s, indicating that the extra coarse grid may not have sufficient control volumes per boundary layer thickness to predict the separation at the exact location. Finally, we also note that the prediction of C_f improves with increased grid resolution, as observed for the pressure coefficient.
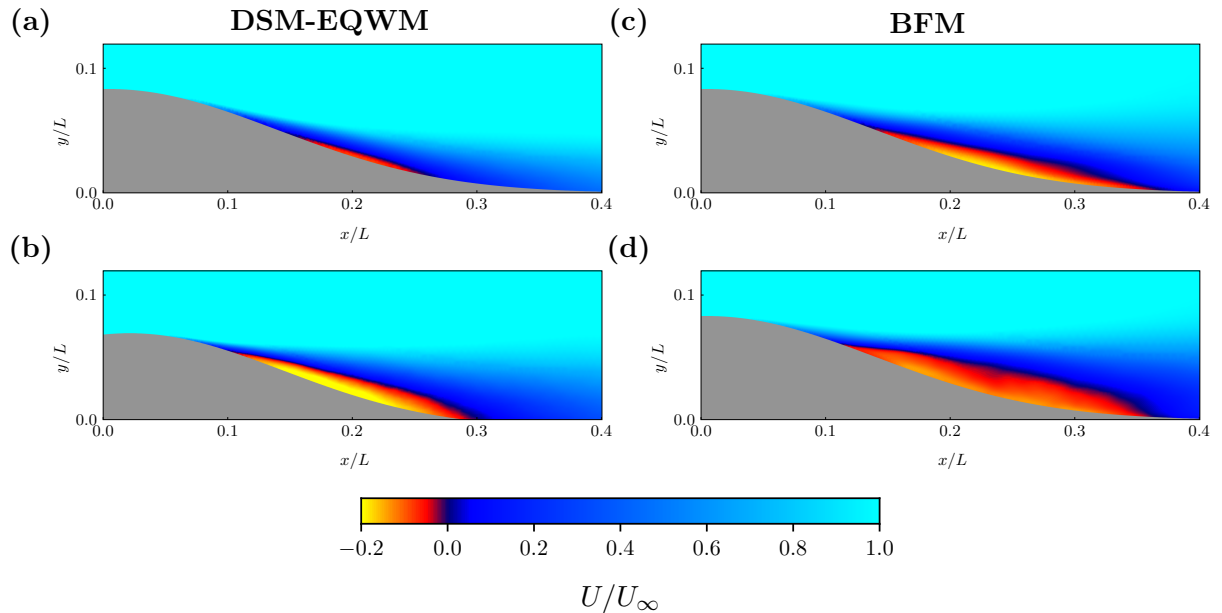
Figure 4-15: Average streamwise velocity (U/U_∞) in the $y/L = 0$ plane for different cases: (a) DSM-EQWM-ExtraC; (b) DSM-EQWM-C; (c) BFM-ExtraC; and (d) BFM-C.

4.3.2.3 Mean Profile

Figure 4-15 displays the average streamwise velocity in the $y/L = 0$ plane for all the cases. The recirculation region corresponds to zones colored in red and yellow. As inferred from C_p and C_f measurements, Fig. 4-15a shows that the DSM-EQWM-ExtraC predicts a small separation bubble. A quantitative improvement is observed for BFM-ExtraC (Fig. 4-15b), although the separation bubble is thinner than the one measured experimentally (see Fig. 9 in [67]). Refining the grid improves the prediction of the separation bubble for both models (compare Fig. 4-15b,d to Fig. 4-15a,c, respectively). In particular, BFM-C provides the separation bubble that resembles the most to the experimental results in terms of size and shape.

By comparing the recirculation regions in Fig. 4-15b and 4-15d, we see that the magnitude of the velocity close to the wall is higher for the DSM-EQWM than for the BFM. Since higher velocities can be linked to a lower pressure and higher (negative) friction coefficients, a likely reason for the smaller values of C_p and C_f predicted by the BFM may be the underprediction of the velocity magnitude in the region with strong APG. To further support this hypothesis, Fig. 4-16 depicts the average velocity profile at selected streamwise locations where experimental data is available [67]. At upstream x_s (probe ①), the flow is attached, and all models provides a velocity profile similar to the experimental mean velocity profile. At the beginning of the separation bubble (probe ②), DSM-EQWM-C predicts a reversal flow stronger than the experiments close to the wall, whereas BFM-C predicts a lower velocity, in line with our hypothesis. As the separation bubble further develops downstream (probe ③), all models fail to capture the strong reversal velocity. This is consistent with the higher pressure and lower friction predicted by the models at $x/L \approx 0.23$. At the second half of the separation bubble (probe ④), the magnitude of the negative velocity close to the wall is milder and is accurately captured by the BFM as opposed to DSM-EQWM, which predicts re-attatched flow.
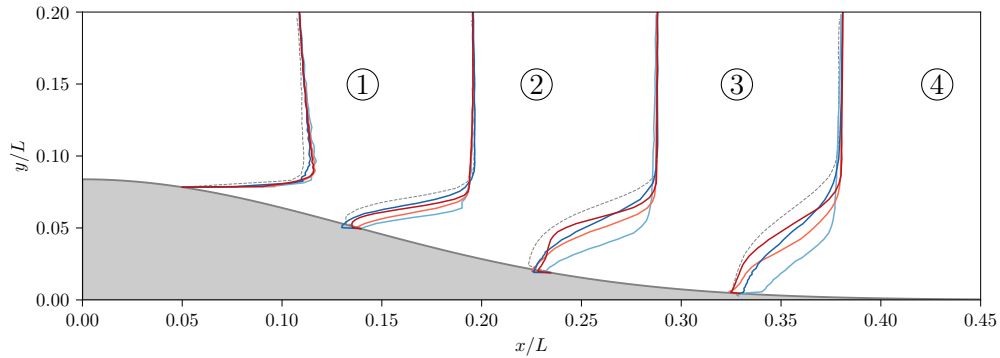
Figure 4-16: Average velocity profile at $y/L = 0$ at different streamwise stations. Line colors correspond to (light blue) DSM-EQWM-ExtraC; (dark blue) DSM-EQWM-C; (light red) BFM-ExtraC; and (dark red) BFM-C cases. Dashed lines correspond to the experimental mean velocity profiles from [67]. Note that $U/U_\infty = 0$ is imposed at the surface to show streamwise location of the probe.

4.3.2.4 Conclusions

Our results show that BFM consistently improves on the prediction of the location and size of the separation bubble when compared to DSM-EQWM simulations. This improvement is particularly noticeable for the coarsest grid tested, where DSM-EQMW predicts almost no separation. Compared to experimental measurements, BFM accurately predicts the pressure and friction in the second half of the separation bubble. However, it yields a higher pressure and lower friction in the first half of the separation bubble. The mismatch was explained by the lower velocities predicted by the SGS model in the regions with a strong flow reversal. To improve model performance, we will continue the training of the model with additional cases accounting for adverse pressure gradient effects. A classifier will also be added to label the type of flow for the control volumes close to the wall, enabling the use of tailored ANNs.

In fact, a new version of the model trained with additional cases representative of flow with favorable pressure gradients named BFM v0.2.7 has shown improved agreement with the experimental data as shown in Figure 4-18 and Figure 4-17.

We do not include the details here because the model is still under active development but it indeed shows that the methodology itself is not at fault. With appropriate implementation, the performance of the model can be vastly improved. Details can

be found in [29].
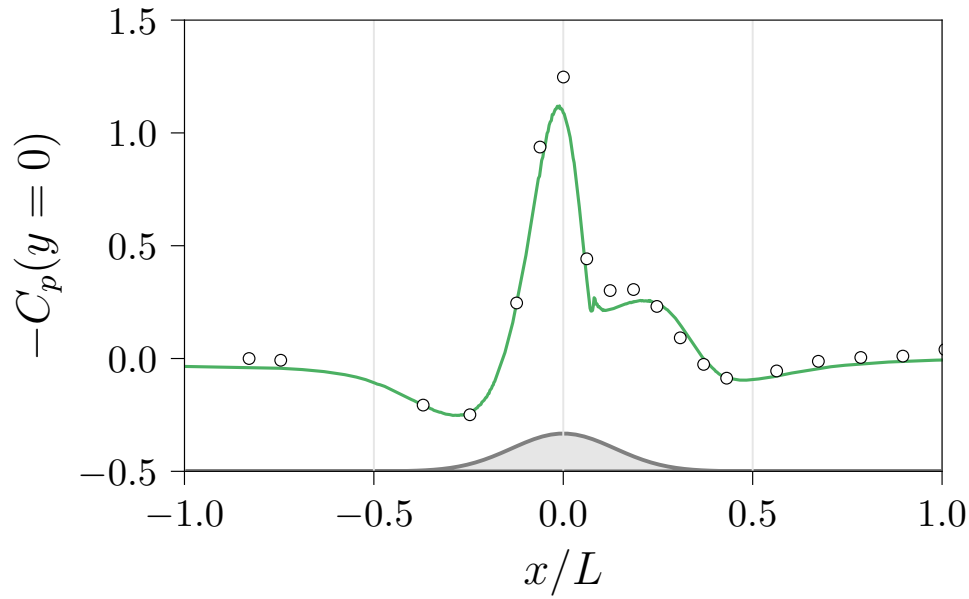
(a)
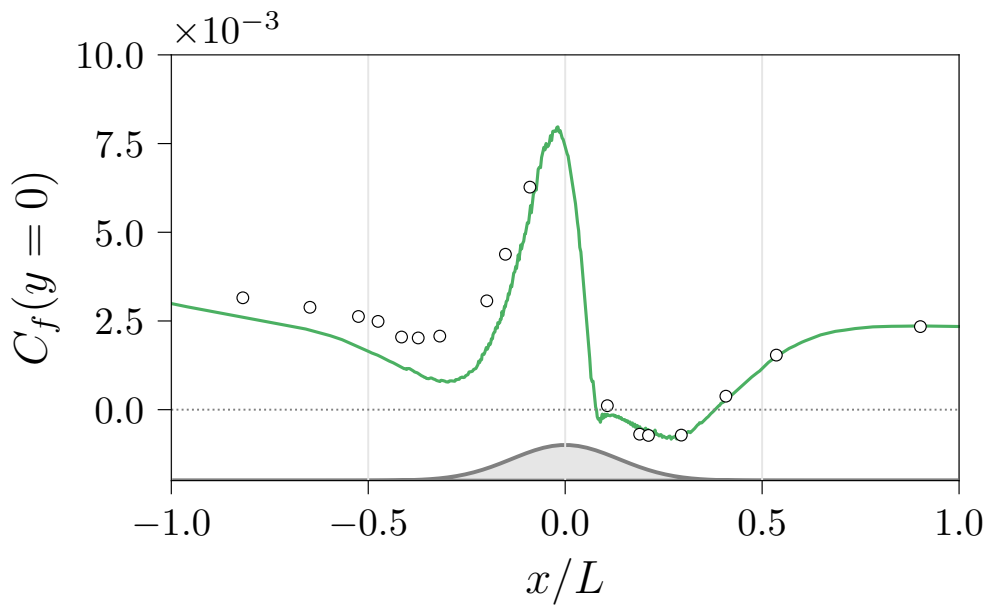
(b)

Figure 4-17: (a) Average pressure coefficients and (b) average friction coefficients over the bump surface at $y/L = 0$ for (Green line) the BFM-v027-ExtraC case. White circles in (a) correspond to experimental results from [65] at $Re_L = 3.41 \times 10^6$, $M = 0.17$, and (b) experimental results from [67] at $Re_L = 2 \times 10^6$, $M = 0.2$.
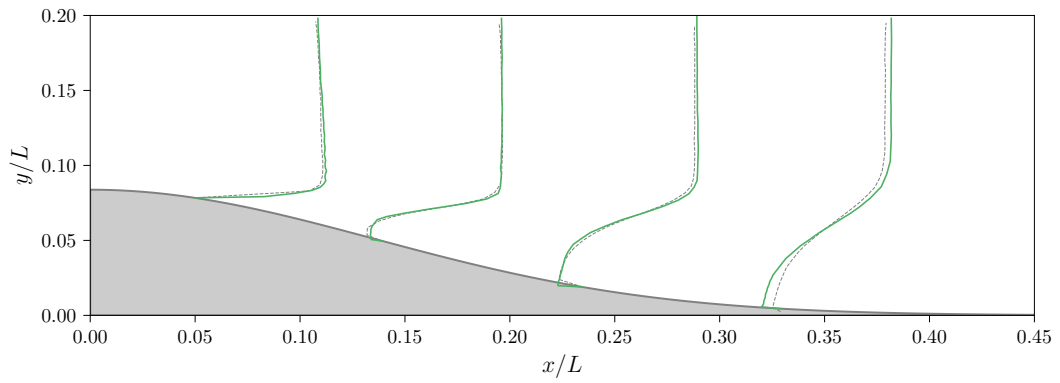
Figure 4-18: Average velocity profile at $y/L = 0$ at different streamwise stations for (Green line) the BFM-v0.2.7-ExtraC case. Dashed lines correspond to the experimental mean velocity profiles from [67]. Note that $U/U_\infty = 0$ is imposed at the surface to show streamwise location of the probe.

Chapter 5

Discussion

5.1 Model Reexamination

In this section, we revisit the model proposed in this thesis and evaluate how well it
meets the original requirements outlined at the beginning of Chapter 3. To reexamine
the model, we will follow the order of the requirements presented in Section 3.1.

(I) Only local in space and time information is required for the current models.
The model has performed better for flows with massive separation compared to
traditional physics-based models.

(II) The model has been trained and applied in the same numerical solvers so that
numerical errors have been dealt with. One exception is the application of BFM
v0.1.0 for CRM-HL. Nonetheless, it still shows better performance. Therefore,
BFM v0.2.0 with training consistent with the numerical schemes is expected to
further improve the performance.

(III) The generalizability of BFMs to different Reynolds numbers has been demon-
strated in cases where Reynolds numbers are different from the training data.

(IV) The model has shown reasonable generalizability to different flow regimes in
validation cases with complex geometries.

(V) The input and output are nondimensionalized consistently with dimensional analysis.

(VI) By using invariants and scalars as model inputs and outputs, the model satisfies this requirement. One exception is the use of the wall-parallel velocity, which is not an invariant. This should be eliminated in the future version of the model.

5.2 Model Limitations

5.2.1 Bousinessq Hypothesis

Eddy viscosity-based models, including the ones discussed in this work, face a limitation associated with the validity of the Boussinesq hypothesis. According to this hypothesis, the SGS stress tensor is assumed to be proportional to the resolved rate of strain tensor. However, this hypothesis has been proven to be incorrect through scaling arguments [68]. Despite this, the Boussinesq hypothesis is widely used in practice due to its simplicity and the fact that it tends to work well in practical applications. One possible explanation for its effectiveness is that the primary objective of modeling the SGS term is to accurately represent the energy dissipation by the subgrid scales, rather than precisely capturing the SGS stress tensor itself [69]. As long as the correct amount of energy is dissipated, the model is expected to perform well. This discrepancy between performance in *a priori* tests (where the model is evaluated against known flow data) and *a posteriori* tests (where the model is evaluated based on its predictive capability) is a crucial aspect to consider. In practical applications, *a posteriori* tests are of paramount importance, and therefore, all results presented in this work are derived from *a posteriori* tests, contrary to some standard testing protocols.

While we refrain from *a priori* tests, finding a non-Boussinesq model that performs well in both *a priori* and *a posteriori* tests would be a significant advancement compared to current eddy viscosity models. Such a model would not only provide improved predictive capabilities but also offer a more accurate physical interpreta-

tion of the underlying flow physics. The ability to reconcile both the theoretical understanding of turbulence and its practical application would contribute to further advancements in the field of turbulence modeling. Therefore, the pursuit of a non-Boussinesq model that excels in both types of tests holds great significance.

Recent research has shown promising results with a new non-Boussinesq model in LES simulations [64]. This model demonstrates the ability to achieve high correlations between exact SGS tensors and resolved rate of strain tensors, while also exhibiting high accuracy in *a posteriori* tests. Moving beyond the Boussinesq hypothesis is indeed a promising direction for future research. However, there are practical constraints in current framework that need to be considered.

Firstly, the controlling strategy would need to adapt to six degrees of freedom (corresponding to a symmetric stress tensor) instead of one as in the case of eddy viscosity. The existing controllers would need significant improvement to handle these additional degrees of freedom effectively and produce satisfactory results. Secondly, the computational cost of the model would likely increase. It remains to be seen how much improvement in computational efficiency is needed to accommodate this increase in cost. Lastly, the inclusion of more training data would be necessary to capture the non-Boussinesq effects. The current training data set is already extensive, and it is unclear how much additional data would be required to adequately represent and capture the non-Boussinesq effects. These practical considerations present challenges that need to be addressed when exploring non-Boussinesq models, but the potential improvements they offer make them a promising avenue for future research.

5.2.2 Training Data

5.2.2.1 Quantity

While training cases as summarized in Table 3.1 are extensive, there is still room for improvement. Indeed, as mentioned in Section 4.3.2.4, a new version of BFM with some additional test cases outperforms the BFM v0.2.0 by a fair margin for the Gaussian bump. Therefore, it seems reasonable to expect that the performance of

the classifier can be further improved by adding more training cases. However, the computational cost of generating training cases, mostly coming from the controller, is a significant limiting factor. The current training data set already requires a substantial amount of computational resources, and it is unclear how much additional data would be needed to achieve a significant improvement in performance. One possible remedy is to quantify the relative importance of each training case so that we can use and select the most meaningful ones instead of naively including all of them. Strategy to carry out such search remains to be explored.

5.2.2.2 Quality

The non-convergence behavior observed in the results also raises concerns regarding the adequacy of the current training dataset in capturing all the necessary flow physics. One potential argument is that phenomena such as separation and reattachment observed in cases with Gaussian bumps may arise from the curvature of the geometry, rather than solely being attributed to the adverse-pressure-gradient effect that is captured in cases with periodic boundary conditions. Although this remains a topic of debate, it does highlight the question of whether a finite set of training cases can effectively represent the diverse range of flow physics encountered in practical applications.

Answering this question requires empirical evaluation through the systematic addition and subtraction of training cases, in order to assess the impact on the model's performance and capability to capture a broader range of flow behaviors. This task represents an important avenue for future research, as it aims to identify the optimal training dataset that sufficiently encompasses the flow physics encountered in various scenarios. By refining the training dataset, we can enhance the model's predictive capabilities and ensure its robustness across a wider range of flow conditions.

5.2.3 Training of ANN

In this thesis, all ANNs are trained using a scaled conjugate gradient backpropogation method, which is considered relatively outdated compared to more advanced optimization techniques such as Adam [70]. The choice of scaled conjugate gradient backpropagation was primarily influenced by the software used for training, which is MATLAB in our case. This choice was made because the trained networks can be exported to plain C files, facilitating seamless integration into either the in-house FORTRAN solver or charLES written in C++. In contrast, other software libraries like TensorFlow and PyTorch do not offer the same level of convenience in this regard. Due to this limitation, we are constrained to using older optimization methods in the shallow neural network implementation provided by MATLAB. As a result, the extent of performance improvements that can be achieved by employing more modern optimization techniques, remains unclear. However, further investigation into the potential benefits of utilizing Adam or other advanced optimization methods would be worthwhile in order to explore possibilities for enhancing the performance of the trained networks.

5.2.4 Grid Convergence

In the field of CFD, the convergence of results as the grid is refined is typically considered an important indicator of code accuracy and reliability. However, in the case of WMLES using the BFM, we observe a decrease in accuracy from extra coarse to coarse grids, indicating a lack of convergence. It is crucial to note that this non-monotonic convergence issue is not specific to our model alone, but is a recognized challenge in the context of WMLES. Nonetheless, it remains necessary to investigate the underlying source of this non-monotonic behavior, particularly as other models do not exhibit the same non-monotonicity with the same coarse grid sizes.

This presents a intricate problem since our primary focus is on achieving better performance for coarse grids, typically with fewer than 20 grid points per boundary layer. Therefore, traditional convergence may not be crucial since finer grids are not of

immediate interest. However, the presence of non-monotonic behavior raises concerns about the model's robustness and reliability. As a result, a careful investigation into this issue is warranted to ensure the model's performance and stability, even for coarse grid resolutions.

5.2.5 Classifier

The performance of the classifier plays a crucial role in determining the overall performance of the model. In the case of BFM v0.1.0, the performance of the classifier is not as satisfactory as initially anticipated. This is evident from the fact that BFM with a "perfect" classifier outperforms the version with the actual classifier. To enhance the performance of the classifier, several potential improvements can be explored, although none of them have been tested yet and should be considered as future work.

One potential avenue for improvement is to investigate the use of alternative inputs that may provide more informative features for the classifier. This could involve incorporating additional flow parameters or utilizing different data preprocessing techniques. Another option is to explore the use of ANNs as an alternative to the current classifier. ANNs have shown promise in various classification tasks and may offer improved performance in the context of BFM. These potential improvements warrant further investigation as part of future work to enhance the performance of the classifier and, subsequently, the overall performance of the BFM model. Finally, incorporating a classifier into newer versions of BFM holds the potential to improve its performance, provided that the classifier itself demonstrates good performance.

5.2.6 Higher-order Statistics

No results of higher-order or multi-point statistics, such as Reynolds stress and spatial correlations, have been presented in this work. This intentional omission is due to the fact that coarsely resolved LES is not expected to accurately capture such statistics. Higher-order statistics play a significant role in various applications, including aeroacoustics, where accurate representation of turbulent structures and their interactions

is crucial.

Therefore, it is important to emphasize that the current model should not be utilized for applications that heavily rely on higher-order or multi-point statistics without further validation and assessment. These statistics require a higher level of fidelity and resolution, typically achieved through higher-resolution simulations or alternative modeling approaches specifically designed for capturing such quantities accurately.

5.2.7 Variables in the past

It has been reported in previous studies that including variables from the past can improve the performance of turbulence forecasting via ANNs [71, 72]. Current model has no such inputs. No attempt has been made to include such inputs in the near future as it might contradict our objective of developing a model that can be easily implemented in existing solvers.

5.2.8 Confidence Score

Previous versions of BFM for SGS can provide confidence scores for each region [46]. This is not implemented in the current version but should be included in the future.

THIS PAGE INTENTIONALLY LEFT BLANK

Chapter 6

Conclusions and Outlook

Simulation of fluid flows is pivotal for the design of many practical engineering devices. For aerodynamics applications, the prediction of integral quantities of interest is one of the most important tasks and a major challenge according to the NASA CFD Vision 2030 [73]. For a reasonable turnaround in the design cycle, hybrid methods, especially WMLES, have shown great promise. However, the widespread use of WMLES has been hindered by the lack of accurate SGS and wall models, among other factors. Current SGS and wall models have faced challenges in accurately capturing the complex flow physics in practical engineering simulations as they often make assumptions that may not fully capture the intricacies of turbulent flows, leading to limitations in their predictive capabilities.

To overcome this issue, we have developed a unified SGS/wall model for WMLES by devising the flow as a collection of building-block flows. The model is referred to as building-block flow model (BFM). It relies on the assumption that the flow physics in arbitrary settings can be traced back to canonical cases.

The BFM employs two types of neural networks: a classifier and a predictor. The classifier is trained to identify the flow physics and categorize the flow into different canonical cases. The predictor, on the other hand, is trained to predict the SGS and wall shear stress based on the classified flow physics. The training data used for BFM are generated through exact-for-the-mean simulations of canonical flows. In this approach, we correct the eddy viscosity of the base model to obtain accurate

mean profiles, effectively accounting for numerical errors.

Four types of flows are used for the BFM training: laminar channel flow, turbulent channel flow with zero pressure gradient, Poiseuille-Couette flow with mild adverse pressure gradient, and Poiseuille-Couette flow close to separation. By training the BFM on these canonical cases, we aimed to capture the essential physics that can be generalized to more complex flow scenarios.

The model has been validated in canonical flows including laminar channel flow, turbulent channel flow, turbulent Poiseuille-Couette flows with different adverse pressure gradients, and more realistic settings including a Gaussian bump and the NASA High-Lift Common Research Model. The BFM has shown excellent accuracy and generalizability, particularly in scenarios involving very coarse grids, which are essential for achieving reasonable turnaround times in practical engineering applications.

Nonetheless, current versions of BFM can still be improved in several ways. First, the extensibility of the BFM provides a promising avenue for further improvement and refinement. Adding more blocking flows representative of canonical flow physics to the reservoir will be helpful for improving the accuracy and generazability of the model. One simple example is the enhancement of BFM v0.2.7 mentioned at the very end of the Gaussian bump section.

Second, to ensure the model's reliability and applicability in practical engineering cases, additional validation and verification in more complex geometries and flow configurations are essential. Some prominent examples include periodic hills [74, 75] and flow over cylinders with different geometries [76, 77].

Regarding the two versions of the model for different solvers, future work should focus on unifying the datasets and model structures to ensure consistency and comparability between the implementations. Moreover, adding capabilities such as providing confidence scores for classification, which has been demonstrated in the wall-model-only version of the model, can further enhance the model's usability in practice [46].

Finally, in terms of fundamental research of the model, it is crucial to identify and separate the sources of errors in the model. Understanding the contribution of each component, i.e., classifiers and predictors, to the overall error will provide valuable

insights for further model development and optimization.

In summary, current status of BFM is promising. It has shown great potential in improving the accuracy and generazability of WMLES for practical engineering applications. With further development and refinement, the BFM can become a powerful tool for engineering design in the future.

THIS PAGE INTENTIONALLY LEFT BLANK

Bibliography

[1] M. Mani and A. J. Dorgan, "A Perspective on the State of Aerospace Computational Fluid Dynamics Technology", Annu. Rev. Fluid Mech. **55**, 431–457 (2023).

[2] A. J. Smits and I. Marusic, "Wall-bounded turbulence", Phys. Today **66**, 25–30 (2013).

[3] D. Levy, K. Laflin, J. Vassberg, E. Tinoco, M. Mani, B. Rider, O. Brodersen, S. Crippa, C. Rumsey, R. Wahls, J. Morrison, D. Mavriplis, and M. Murayama, "Summary of Data from the Fifth AIAA CFD Drag Prediction Workshop", in 51st AIAA Aerospace Sciences Meeting including the New Horizons Forum and Aerospace Exposition (Jan. 2013).

[4] C. L. Rumsey, J. P. Slotnick, M. Long, R. A. Stuever, and T. R. Wayman, "Summary of the First AIAA CFD High-Lift Prediction Workshop", J. Aircr. **48**, 2068–2079 (2011).

[5] C. C. Kiris, A. S. Ghate, O. M. Browne, J. P. Slotnick, and J. Larsson, "HLPW-4/GMGW-3: Wall-Modeled LES and Lattice-Boltzmann Technology Focus Group Workshop Summary", in AIAA Aviation 2022 Forum (June 2022).

[6] C. L. Rumsey, J. P. Slotnick, and A. J. Sclafani, "Overview and Summary of the Third AIAA High Lift Prediction Workshop", J. Aircr. **56**, 621–644 (2019).

[7] P. Sagaut, *Large eddy simulation for incompressible flows: an introduction*, 3rd ed, Scientific Computation (Springer, 2006).

[8] S. T. Bose and G. I. Park, "Wall-Modeled Large-Eddy Simulation for Complex Turbulent Flows", Annu. Rev. Fluid Mech. **50**, 535–561 (2018).

[9] J. Larsson, S. Kawai, J. Bodart, and I. Bermejo-Moreno, "Large eddy simulation with modeled wall-stress: recent progress and future directions", Mech. Eng. Rev. **3**, 15-00418-15–00418 (2016).

[10] P. R. Spalart, "Detached-Eddy Simulation", Annu. Rev. Fluid Mech. **41**, 181–202 (2009).

[11] J. Fröhlich and D. von Terzi, "Hybrid LES/RANS methods for the simulation of turbulent flows", Prog. Aerosp. Sci. **44**, 349–377 (2008).

[12] U. Piomelli, E. Balaras, H. Pasinato, K. D. Squires, and P. R. Spalart, "The inner–outer layer interface in large-eddy simulations with wall-layer models", Int. J. Heat Fluid Flow **24**, 538–550 (2003).

[13] L. Fu, M. Karp, S. T. Bose, P. Moin, and J. Urzay, "Shock-induced heating and transition to turbulence in a hypersonic boundary layer", J. Fluid Mech. **909**, A8 (2021).

[14] X. I. A. Yang and K. P. Griffin, "Grid-point and time-step requirements for direct numerical simulation and large-eddy simulation", Phys. Fluids **33**, 015108 (2021).

[15] D. R. Chapman, "Computational Aerodynamics Development and Outlook", AIAA J. **17**, 1293–1313 (1979).

[16] H. Choi and P. Moin, "Grid-point requirements for large eddy simulation: Chapman's estimates revisited", Phys. Fluids **24**, 011702 (2012).

[17] K. A. Goc, O. Lehmkuhl, G. I. Park, S. T. Bose, and P. Moin, "Large eddy simulation of aircraft at affordable cost: a milestone in computational fluid dynamics", Flow **1**, E14 (2021).

[18] A. Lozano-Durán, S. T. Bose, and P. Moin, "Performance of Wall-Modeled LES with Boundary-Layer-Conforming Grids for External Aerodynamics", AIAA J. **60**, 747–766 (2022).

[19] S. Brunton, B. Noack, and P. Koumoutsakos, "Machine Learning for Fluid Mechanics", Annu. Rev. Fluid Mech. **52**, 477–508 (2020).

[20] K. Duraisamy, G. Iaccarino, and H. Xiao, "Turbulence Modeling in the Age of Data", Annu. Rev. Fluid Mech. **51**, 357–377 (2019).

[21] M. Gamahara and Y. Hattori, "Searching for turbulence models by artificial neural network", Phys. Rev. Fluids **2**, 054604 (2017).

[22] C. Xie, J. Wang, H. Li, M. Wan, and S. Chen, "Artificial neural network mixed model for large eddy simulation of compressible isotropic turbulence", Phys. Fluids **31**, 085112 (2019).

[23] X. I. A. Yang, S. Zafar, J.-X. Wang, and H. Xiao, "Predictive large-eddy-simulation wall modeling via physics-informed neural networks", Phys. Rev. Fluids **4**, 034602 (2019).

[24] Z. Zhou, G. He, and X. Yang, "Wall model based on neural networks for LES of turbulent flows over periodic hills", Phys. Rev. Fluids **6**, 054610 (2021).

[25] R. Zangeneh, "Data-driven model for improving wall-modeled large-eddy simulation of supersonic turbulent flows with separation", Phys. Fluids **33**, 126103 (2021).

[26] X. Huang, X. Yang, and R. Kunz, "Wall-modeled large-eddy simulations of spanwise rotating turbulent channels—Comparing a physics-based approach and a data-based approach", Phys. Fluids **31**, 125105 (2019).

[27] H. J. Bae and P. Koumoutsakos, "Scientific multi-agent reinforcement learning for wall-models of turbulent flows", Nat. Commun. **13**, 1443 (2022).

[28] Y. Ling, G. Arranz, E. Williams, K. Goc, K. Griffin, and A. Lozano-Durán, "Wall-modeled large-eddy simulation based on building-block flows", in Proceedings of the 2022 Summer Program (Dec. 2022), pp. 5–24.

[29] G. Arranz, Y. Ling, and A. Lozano-Durán, "Correction: Wall-modeled LES based on building-block flows: Application to the Gaussian Bump", in AIAA Aviation 2023 Forum (June 2023).

[30] A. Lozano-Durán, G. Arranz, and Y. Ling, "Building-Block-Flow Model for Large-Eddy Simulation: Application to NASA CRM-HL", in AIAA Aviation 2023 Forum (June 2023).

[31] J. Smagorinsky, "General Circulation Experiments with the Primitive Equations I. The Basic Experiment", Mon. Weather Rev. **91**, 99–164 (1963).

[32] M. Germano, U. Piomelli, P. Moin, and W. H. Cabot, "A dynamic subgrid-scale eddy viscosity model", Phys. Fluids A: Fluid Dyn. **3**, 1760–1765 (1991).

[33] D. K. Lilly, "A proposed modification of the Germano subgrid-scale closure method", Phys. Fluids A: Fluid Dyn. **4**, 633–635 (1992).

[34] S. B. Pope, *Turbulent flows* (Cambridge university press, 2000).

[35] B. Vreman, B. Geurts, and H. Kuerten, "Large-eddy simulation of the turbulent mixing layer", J. Fluid Mech. **339**, 357–390 (1997).

[36] A. W. Vreman, "An eddy-viscosity subgrid-scale model for turbulent shear flow: Algebraic theory and applications", Phys. Fluids **16**, 3670–3681 (2004).

[37] R. Verstappen, "When Does Eddy Viscosity Damp Subfilter Scales Sufficiently?", J. Sci. Comput. **49**, 94–110 (2011).

[38] W. Rozema, H. J. Bae, P. Moin, and R. Verstappen, "Minimum-dissipation models for large-eddy simulation", Phys. Fluids **27**, 085107 (2015).

[39] C. M. Bishop, *Pattern recognition and machine learning*, Information Science and Statistics (Springer, 2006).

[40] K. Hornik, M. Stinchcombe, and H. White, "Multilayer feedforward networks are universal approximators", Neural Netw. **2**, 359–366 (1989).

[41] P. Orlandi and R. Moreau, eds., *Fluid Flow Phenomena*, Vol. 55, Fluid Mechanics and Its Applications (Springer Netherlands, 2000).

[42] A. Wray, *Minimal-storage time advancement schemes for spectral methods*, NASA Ames Research Center, California, Report No. MS (NASA Ames Research Center, 1990).

[43] H. J. Bae, A. Lozano-Durán, S. T. Bose, and P. Moin, "Turbulence intensities in large-eddy simulation of wall-bounded flows", Phys. Rev. Fluids **3**, 014610 (2018).

[44] G. A. Brès, S. T. Bose, M. Emory, F. E. Ham, O. T. Schmidt, G. Rigas, and T. Colonius, "Large-eddy simulations of co-annular turbulent jet using a Voronoi-based mesh generation framework", in 2018 AIAA/CEAS Aeroacoustics Conference (June 2018).

[45] A. Lozano-Durán and H. J. Bae, *Self-critical machine-learning wall-modeled LES for external aerodynamics*, May 2021.

[46] A. Lozano-Durán and H. J. Bae, "Machine learning building-block-flow wall model for large-eddy simulation", J. Fluid Mech. **963**, A35 (2023).

[47] T. S. Lund, "Parameterization of subgrid-scale stress by the ve locity gradient tensor.", in Annual Research Briefs (1992), pp. 27–43.

[48] S. B. Pope, "A more general effective-viscosity hypothesis", J. Fluid Mech. **72**, 331 (1975).

[49] H. J. Bae and A. Lozano-Durán, "Effect of Wall Boundary Conditions on a Wall-Modeled Large-Eddy Simulation in a Finite-Difference Framework", Fluids **6**, 112 (2021).

[50] M. Pelikan and M. Pelikan, *Hierarchical Bayesian Optimization Algorithm: Toward a New Generation of Evolutionary Algorithms*, Hierarchical Bayesian Optimization Algorithm 170 (Springer-Verlag, 2005).

[51] J. C. Del Lamo, J. Jimnez, P. Zandonade, and R. D. Moser, "Scaling of the energy spectra of turbulent channels", J. Fluid Mech. **500**, 135–144 (2004).

[52] S. Hoyas and J. Jiménez, "Scaling of the velocity fluctuations in turbulent channels up to Reτ=2003", Phys. Fluids **18**, 011702 (2006).

[53] A. Lozano-Durán and J. Jiménez, "Effect of the computational domain on direct simulations of turbulent channels up to Reτ≈4200", Phys. Fluids **26**, 011702 (2014).

[54] S. Hoyas, M. Oberlack, F. Alcántara-Ávila, S. V. Kraheberger, and J. Laux, "Wall turbulence at high friction Reynolds numbers", Phys. Rev. Fluids **7**, 014602 (2022).

[55] I. Marusic, J. P. Monty, M. Hultmark, and A. J. Smits, "On the logarithmic region in wall turbulence", J. Fluid Mech. **716**, 10.1017/jfm.2012.511 (2013).

[56] D. S. Lacy and A. J. Sclafani, "Development of the High Lift Common Research Model (HL-CRM): A Representative High Lift Configuration for Transonic Transports", in 54th AIAA Aerospace Sciences Meeting (Jan. 2016).

[57] T. Ito, Y. Yokokawa, H. Ura, H. Kato, K. Mitsuo, and K. Yamamoto, "High-Lift Device Testing in JAXA 6.5M X 5.5M Low-Speed Wind Tunnel", in 25th AIAA Aerodynamic Measurement Technology and Ground Testing Conference (June 2006).

[58] K. Goc, S. T. Bose, and P. Moin, "Large Eddy Simulation of the NASA High-Lift Common Research Model", in AIAA Scitech 2022 Forum (Jan. 2022).

[59] A. N. Evans, D. S. Lacy, I. Smith, and M. B. Rivers, "Test Summary of the NASA High-Lift Common Research Model Half-Span at QinetiQ 5-Metre Pressurized Low-Speed Wind Tunnel", in AIAA Aviation 2020 Forum (June 2020).

[60] T. Poinsot and S. Lelef, "Boundary conditions for direct simulations of compressible viscous flows", J. Comput. Phys. **101**, 104–129 (1992).

[61] A. Uzun and M. R. Malik, "Simulation of a turbulent flow subjected to favorable and adverse pressure gradients", Theor. Comput. Fluid Dyn. **35**, 293–329 (2021).

[62] P. S. Iyer and M. R. Malik, "Wall-modeled LES of flow over a Gaussian bump", in AIAA Scitech 2021 Forum (Jan. 2021).

[63]P. S. Iyer and M. R. Malik, "Wall-modeled LES of the Three-dimensional Speed Bump Experiment", in AIAA Scitech 2023 Forum (Jan. 2023).

[64]R. Agrawal, M. P. Whitmore, K. P. Griffin, S. T. Bose, and P. Moin, "Non-Boussinesq subgrid-scale model with dynamic tensorial coefficients", Phys. Rev. Fluids **7**, 074602 (2022).

[65]O. Williams, M. Samuell, E. S. Sarwas, M. Robbins, and A. Ferrante, "Experimental Study of a CFD Validation Test Case for Turbulent Separated Flows", in AIAA Scitech 2020 Forum (Jan. 2020).

[66]G. Arranz, Y. Ling, and A. Lozano-Durán, "Wall-modeled LES based on building-block flows: Application to the Gaussian Bump", in AIAA Aviation 2023 Forum (June 2023).

[67]P. D. Gray, I. Gluzman, F. O. Thomas, and T. C. Corke, "Experimental Characterization of Smooth Body Flow Separation Over Wall-Mounted Gaussian Bump", in AIAA Scitech 2022 Forum (Jan. 2022).

[68]H. Tennekes and J. L. Lumley, *A first course in turbulence* (MIT Press, 1972).

[69]W. Rozema, "Low-dissipation methods and models for the simulation of turbulent subsonic flow: theory and applications", PhD thesis (University of Groningen, 2015).

[70]D. P. Kingma and J. Ba, *Adam: A Method for Stochastic Optimization*, Jan. 2017.

[71]P. A. Srinivasan, L. Guastoni, H. Azizpour, P. Schlatter, and R. Vinuesa, "Predictions of turbulent shear flows using deep neural networks", Phys. Rev. Fluids **4**, 054603 (2019).

[72]A. Lozano-Durán, H. J. Bae, and M. P. Encinar, "Causality of energy-containing eddies in wall turbulence", J. Fluid Mech. **882**, A2 (2020).

[73]J. P. Slotnick, A. Khodadoust, J. Alonso, D. Darmofal, W. Gropp, E. Lurie, and D. J. Mavriplis, *CFD Vision 2030 Study: A Path to Revolutionary Computational Aerosciences*, tech. rep. NF1676L-18332 (Boeing Research & Technology, Mar. 2014).

[74]B. Krank, M. Kronbichler, and W. A. Wall, "Direct Numerical Simulation of Flow over Periodic Hills up to ReH = 10,595", Flow Turbul. Combust. **101**, 521–551 (2018).

[75]H. Xiao, J.-L. Wu, S. Laizet, and L. Duan, "Flows over periodic hills of parameterized geometries: A dataset for data-driven turbulence modeling from direct simulations", Comput. Fluids **200**, 104431 (2020).

[76]F. Trias, A. Gorobets, and A. Oliva, "Turbulent flow around a square cylinder at Reynolds number 22,000: A DNS study", Comput. Fluids **123**, 87–98 (2015).

[77]S. Dong and G. Karniadakis, "DNS of flow past a stationary and oscillating cylinder at", J. Fluids Struct. **20**, 519–531 (2005).